Ground solar absorption observations of total column CO, CO_2, CH_4, and aerosol optical depth from California's Sequoia Lightning Complex Fire: Emission factors and modified combustion efficiency at regional scales

Isis Frausto-Vicencio[1], Sajjan Heerah[2], Aaron G. Meyer[2], Harrison A. Parker[3], Manvendra Dubey[2] and Francesca M. Hopkins[1]

[1]Department of Environmental Sciences, University of California, Riverside, 92507, USA
[2]Los Alamos National Laboratory, Los Alamos, 87545, USA
[3]California Institute of Technology, Pasadena, 91125, USA

Correspondence to: Isis Frausto-Vicencio (ifrau001@ucr.edu)

Abstract. With global wildfires becoming more widespread and severe, tracking their emissions of greenhouse gases and air pollutants is becoming increasingly important. Wildfire emissions have primarily been characterized by *in situ* laboratory and field observations at fine scales. While this approach captures the mechanisms relating emissions to combustion phase and fuel properties, their evaluation on regional scale plumes has been limited. In this study, we report remote observations of total column trace gases and aerosols in the 2020 wildfire season of smoke plumes from the Sierra Nevada of California with an EM27/SUN solar Fourier transform infrared (FTIR) spectrometer. We derive total column aerosol optical depth (AOD), emission factors (EF) and modified combustion efficiency (MCE) for these fires, and evaluate relationships between them based on combustion phase at regional scales. We demonstrate that the EM27/SUN effectively detects changes of CO, CO_2 and CH_4 in the atmospheric column at ~10 km horizontal scales that are attributed to wildfire emissions. These observations are used to derive total column EF_{CO} of 120.5 ± 12.2 and EF_{CH4} of 4.3 ± 0.8 for a regional smoke plume event in mixed combustion phases. These values are consistent with *in situ* relationships measured in similar temperate coniferous forest wildfires. FTIR-derived AOD was compared to a nearby AERONET station and observed ratios of AOD to X_{CO} were consistent with those previously observed from satellites. We also show that co-located X_{CO} observations from the TROPOMI satellite-based instrument are $9.7 \pm 1.3\%$ higher than our EM27/SUN observations during the wildfire period. Finally, we put wildfire CH_4 emissions in context of the California state CH_4 budget and estimate that 213.7 ± 49.8 Gg CH_4 were emitted by large wildfires in California during 2020, about 13.7% of the total state CH_4 emissions in 2020. Our work demonstrates a novel application of the ground-based EM27/SUN solar spectrometers in wildfire monitoring by integrating regional scale measurements of trace gases and aerosols from smoke plumes.

1 Introduction

Wildfires have become deadlier, more destructive, and more frequent globally over the past few years (UNEP, 2022). Particularly, the 2020 wildfire activity season surged with massive wildfires in the Western U.S., Australia, Brazil, and the Arctic. The California 2020 wildfire season was exacerbated by abnormally high temperatures and dry conditions (Jain et al.,

2022; Cho et al., 2022) and emitted ten times more carbon dioxide into the atmosphere than the 2000-2019 annual average (CARB, 2020). In the San Joaquin Valley (SJV) of California, atmospheric concentrations of fine particles that are 2.5 microns

35   or smaller in size, also known as particulate matter 2.5 ($PM_{2.5}$), were found to be four times higher during the 2020 fire season than non-fire periods (Ahangar et al., 2022). The high temperatures and dry conditions, combined with moisture from a tropical storm led to a dry lightning storm event in August 2020, where lightning-ignited wildfires burned more acres in California than at any other time in recorded history (Morris III and Dennis, 2020). This included the lightning-sparked Castle Fire (part of the Sequoia Lightning Fire (SQF) Complex) that killed 10-14% of the large sequoias in the Sierra Nevada and has become

40   the largest fire in a giant sequoia grove on record (Stephensen and Brigham, 2021). Historic fire suppression and land-use changes in this area has led to an increase of wildfires burning at higher intensity and larger areas (Moody et al., 2006; Scholl and Taylor, 2010). Climate change has increased the forest fire activity in the Western U.S. (Zhuang et al., 2021) and will increase the likelihood of wildfires in the Sierra Nevada with greater burned area due to higher daily temperatures (Gutierrez et al., 2021), and implications for air quality and carbon emissions (Navarro et al., 2016).

45   Wildfires are a major source of air pollutants, including particulate matter (PM), carbon monoxide (CO), and greenhouse gases, primarily carbon dioxide (CO_2) and methane (CH_4) (Akagi et al., 2011; Wiedinmyer et al., 2011; Andreae, 2019). The high levels of PM and CO released from fires are dangerous to human health and degrade air quality on a local, regional, and global scale (Schneising et al., 2020; Aguilera et al., 2021). CO is an air toxic and is considered an indirect greenhouse gas as it is a major sink for the hydroxyl radical (OH), increasing the abundance of CH_4 through photochemical

50   feedbacks (Li et al., 2018) and also produces ozone (O_3), a short lived greenhouse gas. CO_2 and CH_4 are the dominant greenhouse gases and are responsible for most of the current anthropogenic climate change (IPCC, 2021). Although emissions from fires are biogenic sources of CO_2, they are released rapidly compared to the slow timescales of carbon uptake required to grow vegetation fuels. Increased fire activity increases atmospheric CO_2 in the short term, and can locally alter the terrestrial carbon cycle balance by reducing photosynthetic CO_2 uptake due to high levels of vegetation disturbance (Lasslop et al., 2019).

55   While CO_2 losses can be estimated as a function of burned area and fuel consumption, emissions of CO, CH_4, and aerosols are more difficult to estimate because they vary greatly with wildfire combustion phases. As global wildfires become more widespread and severe, tracking emissions of greenhouse gases and air pollutants from smoke will become increasingly important for efforts to track emissions of greenhouse gases and understand the impacts of fire on the atmosphere (Aguilera et al., 2021; Wilmot et al., 2022).

60   Our understanding of the atmospheric impacts of increasing fire activity relies on accurate observations and process-based estimation of fire emissions that have been developed using *in situ* measurements (Urbanski, 2014). While several space-based instruments can retrieve and derive emissions of important trace gases globally, observations of trace gases are limited by spatiotemporal coverage and aerosol burden from smoke plumes (Schneising et al., 2020). Recent satellite studies have focused on trace gas emissions and ratios for CH_4, CO, nitrogen oxides (NO_x) and ammonia (NH_3) (Whitburn et al., 2015;

65   Adams et al., 2019; Griffin et al., 2021; Jin et al., 2021), but few focus on the integration of trace gases and aerosols. Ground-based solar spectrometers present an alternative technique to measure and understand fire emissions at regional scales, and

temporally complement satellite observations. Column measurements are insensitive to the planetary boundary layer growth and are less affected by nearby point sources than *in situ* measurements, making them a good candidate for regional-scale monitoring (Lindenmaier et al., 2014). The EM27/SUN is a ground-based remote sensing instrument that is relatively portable

70   and robust for field deployments (Chen et al., 2016; Heerah et al., 2021). These instruments are the basis for the ground-based network of Fourier Transform Infrared (FTIR) COCCON (COllaborative Carbon Column Observing Network) (Frey et al., 2019; Vogel et al., 2019; Alberti et al., 2022a, b), which complements NDACC (Network for the Detection of Atmospheric Composition Change) (Bader et al., 2017; De Mazière et al., 2018) and TCCON (Total Column Carbon Observing Network), two high resolution FTIR trace gas monitoring networks (Toon et al., 2009; Wunch et al., 2011).

75   Field-based measurements of biomass burning in temperate forests are limited and sparse (Burling et al., 2011; Urbanski, 2014), despite the increase in burning activity in the Western U.S. (Zhuang et al., 2021). The EM27/SUN provides vertically integrated column measurements of CH_4, CO_2, and CO which allows for calculating modified combustion efficiency (MCE) and emission factors (EFs) in the total column of smoke plumes downwind of wildfires. MCE values give insight into the relative amounts of flaming and smoldering combustion of the fire. EFs are defined as the mass of gas or aerosol emitted

80   per dry biomass consumed and are critical inputs for models to accurately calculate emissions and construct wildfire inventories (Urbanski, 2014). Providing new EFs will help improve regional biomass burning estimates. Past studies have derived atmospheric column-based EFs with respect to CO from wildfires using solar FTIR spectrometers (Paton-Walsh et al., 2005; Viatte et al., 2014, 2015; Lutsch et al., 2016, 2020; Kille et al., 2022). The observed small changes in CO_2 with respect to the large atmospheric background has limited previous FTIR-based studies in their ability to derive EFs with respect to CO_2. This

85   has consequently inhibited the calculation of MCE. Here, we present the first EFs with respect to CO_2 and MCE for wildfires calculated by total column FTIR.
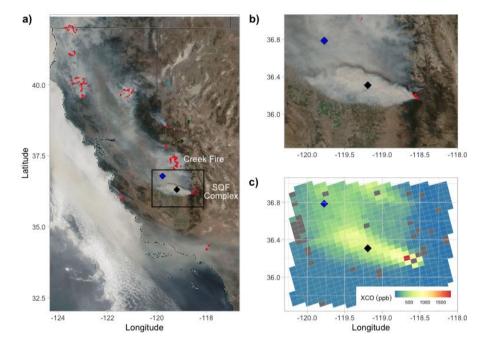
        During part of the 2020 wildfire season, we deployed the EM27/SUN in the SJV downwind of two major Sierra Nevada wildfires, SQF Complex and Creek Fire. We report EF_{CO} and EF_{CH4} from the SQF Complex, a mixed conifer forest wildfire, and calculate the wildfire's combustion phase with MCE values. We also derived AOD from the EM27/SUN solar

90   spectra and compare to a nearby AERONET site. Furthermore, because ground-based column measurements operate on similar scales as satellites (McKain et al., 2015), we compared EM27/SUN measurements with observations of CO from TROPOspheric Monitoring Instrument (TROPOMI) collected during the fires. Finally, using enhancement ratios we estimate wildfire CH_4 emissions for 2020 and put our 2020 wildfire CH_4 emission estimates in context of the California state CH_4 budget.

95   **2 Data Sources and Methods**

        We measured the column-averaged dry air mole fractions (X_{gas}) of CH_4, CO_2 and CO (X_{CH4}, X_{CO2}, and X_{CO}) with the EM27/SUN at a site downwind of two major fires in the Sierra Nevada: SQF Complex and Creek Fire. We also derived AOD from the measured solar spectra of the EM27/SUN and compare to a nearby AERONET site (Figure 1). The measurement site was located 60 km west of the SQF Complex that was composed of the Castle and Shotgun fires, and 80 km south of the Creek

100 wildfire (Figure 1, panel a). The SQF Complex fires began on Aug. 19, 2020, after a dry thunderstorm and lightning event ignited the fires in the Sierra Nevada. By Sept. 12 the SQF Complex had grown to 283 km^2 and a large wildfire plume from this fire traveled west directly over our measurement site that was captured by the EM27/SUN and TROPOMI (Figure 1, panel b and c). The Creek Fire began on the evening of Sept. 5 and upper-level high winds produced a pyro-cumulus cloud on Sept. 6 that reached an altitude over 15 km (Morris III and Dennis, 2020). Smoke filled the valley and smoky overcast skies remained

105 in large parts of the SJV for the next two weeks as fires kept burning. In total, the SQF Complex consumed 686 km^2 and Creek consumed 1515 km^2, placing both these fires among the 20 largest California wildfires ever recorded (Morris III and Dennis, 2020).

110 **Figure 1.** a) Satellite imagery captured by NOAA-20 VIIRS of heavy smoke in California on Sept. 12, 2020, highlighting fire and thermal anomalies in red (NASA Worldview; worldview.earthdata.nasa.gov), and with black diamond shape showing the EM27/SUN measurement location and blue diamond shape showing the AERONET observational site. b) Inset shows more detail of the smoke plume within the SJV from the SQF Complex in the Sierra Nevada. c) Inset of TROPOMI X_{CO} overpass at 2020-09-12 13:54 PDT.

115

2.1 EM27/SUN Atmospheric Column Observations

The Bruker Optics EM27/SUN solar-viewing Fourier transform spectrometer owned by Los Alamos National Laboratory (LANL) collected continuous daytime column measurements in Farmersville, California (36.31, -119.19) from Sept. 8 until Oct. 17, 2020, for a total of 40 days of observations. EM27/SUN X_{gas} values were retrieved from unaveraged

120　double sided interferograms using the I2S and GFIT (GGG2014 version; https://tccon-wiki.caltech.edu/) retrieval algorithms automated by the EGI processing suite (Hedelius et al., 2016). Surface pressure is required to retrieve dry air columns in GGG and we used Coastal Environmental Systems ZENO weather station to record surface pressure at our field site for retrievals. Retrievals also require atmospheric profiles of temperature, pressure, altitude and water and these profiles were extracted from NCEP/NCAR reanalysis product (Kalnay et al., 1996). We calibrated the EM27/SUN via co-located measurements alongside

125　the IFS125, a high spectral resolution FTIR operated by TCCON at the California Institute of Technology (CIT), both before and after the collection periods to determine calibration factors (R_{gas}) assuming a linear model forced through the origin for each gas, e.g., $X_{TCCON} = X_{EM27} R_{gas}$ (Chen et al., 2016; Hedelius et al., 2016). The TCCON network sets the standard as the current state-of the art ground-based validation system for remote sensing and satellite-based observations of greenhouse gases (Wunch et al., 2011), and TCCON observations are tied to the World Meteorological Organization (WMO) standard

130　greenhouse gas scale. Co-locating the EM27/SUN and TCCON instruments ensures system stability of the EM27/SUN after transportation to field sites. Co-located measurements were performed on Sept. 2 – 3, 2020 and Oct. 30 – Nov. 1, 2020. Results of the correction factors from the co-located measurements are shown in Table A1 of the Appendix. The TCCON instrument also uses the GFIT retrieval algorithm with the same *a priori* profiles; however, due to different instrument spectral resolutions and averaging kernels, we correct for the differences between the EM27/SUN and TCCON instrument following Hedelius et

135　al. (2016) (Equation A4) to adjust the EM27/SUN retrievals before comparing with TCCON and deriving calibration factors.

　　　　The EM27/SUN solar spectrometer has been previously used to study emissions from urban and agriculture CH_4 and CO_2 sources (Chen et al., 2016; Viatte et al., 2017; Dietrich et al., 2021; Heerah et al., 2021; Makarova et al., 2021; Alberti et al., 2022a). The recent addition of a CO detector in Bruker's EM27/SUN FTIR spectrometer increases the instrument's utility for measuring combustion sources and as a validation tool for TROPOMI column X_{CO} as it covers the same spectral region

140　(Hase et al., 2016). The EM27/SUN uses the sun as the light source which allows it to derive aerosol optical depth (AOD) as demonstrated by Barreto et al. (2020) at the TCCON FTIR and AERONET site in Izaña, Spain. In their study, TCCON spectra were degraded to the same resolution as the EM27/SUN (0.5 cm^{-1}) and it was concluded that EM27/SUN spectra would be able to effectively derive AOD. Following their approach, we derive AOD for the wildfire period from our measurements. Further details of the AOD calculation are found in Appendix B.

145　　　　Prior to measurements in California, the EM27/SUN was stationed in Fairbanks, Alaska for several months. Given the different settings used with the CamTracker, the solar disk was not centered on the camera and this misalignment was found on Sept. 7. Based on co-located measurements with the CIT TCCON on Sept. 2 and 3, it was determined that the observations within the second detector of X_{CO} were affected on the days prior when camera was misaligned (Sept. 2, 3, 6, and 7). For this reason, we report measurements of X_{CO}, X_{CO2} and X_{CH4} beginning on Sept. 8 and use the Oct. 30 – Nov. 1 co-

150　located measurements for calculating correction factors. AOD was derived from micro-windows within the first detector, thus calculations of AOD were not affected.

2.2 TROPOMI CO Column Measurements

TROPOMI is an instrument launched in late 2017 onboard the European Space Agency's (ESA) Sentinel-5-Precursor (S5P). The instrument measures Earth radiance spectra in the ultraviolet, near infrared, and shortwave infrared allowing for measurements of a wide range of atmospheric trace gases and aerosol properties (Veefkind et al., 2012). The satellite has a sun-synchronous orbit with daily global coverage and a spatial resolution of 5.5 x 7 km^2 for CH_4 and CO operational level 2 (L2) products. The offline (OFFL) CO total column L2 data product filtered for quality assurance values > 0.5 are used in this work as recommended in the product readme file (https://sentinel.esa.int/documents/247904/3541451/Sentinel-5P-Carbon-Monoxide-Level-2-Product-Readme-File, last access: 4 Aug 2022). This selection filters out high solar zenith angles, any corrupted retrievals, and influences from high clouds. The majority of the TROPOMI X_{CH4} product was flagged out near the observational site during our measurement period, and hence was not included in this analysis. Following Sha et al. (2021), the TROPOMI CO column densities were converted to X_{CO} (ppb) by using the modeled surface pressure and total column of water to calculate the column of dry air.

There is growing intertest in using the TROPOMI X_{CO} product for understanding global wildfire fluxes, however few studies focus on evaluating those observations (e.g., Jacobs 2021 and Rowe et al., 2021). We measured a range of X_{CO} levels of mixed smoke plumes and were able to isolate a concentrated smoke plume from a nearby fire. This allowed for a ground-based evaluation of the TROPOMI sensor under various wildfire conditions, including high X_{CO} and aerosol loading in the atmosphere. A correction factor was calculated for the EM27/SUN to account for differences in the *a priori* profile used in the retrieval of X_{CO} in both instruments. We follow the *a priori* substitution method described in Jacobs (2021) and Sha et al. (2021) to calculate an additive factor for the EM27/SUN. Due to the possibility of measuring narrow smoke plumes on subgrid spatiotemporal scales, we perform a sensitivity study to determine the best co-location criteria for the EM27/SUN to TROPOMI comparison by varying the maximum radius (5 – 50 km) from the observational site and averaging time (5 – 30 min) for the EM27/SUN measurements around the TROPOMI overpass time. We required a minimum threshold of at least three 1-minute averages within the averaging time aggregations.

2.3 AERONET Data

AERONET (http://aeronet.gsfc.nasa.gov/, accessed on 15 June 2022) is a global network of sun/sky radiometer with over 600 sites operated around the globe. AERONET observations include measurements of AOD, microphysical, and radiative properties. The stations are frequently calibrated, and they set the standard for aerosol measurements and validation for satellite products (Giles et al., 2019). AERONET measures AOD at several spectral windows from 340, 380, 440, 500, 675, 870, 940, 1020 and 1640 nm. The Ångström exponent (AE), describing the wavelength dependence of aerosol optical thickness, is calculated from the spectral AOD. We used the AERONET Level 2.0 version 3 AOD and AE data from the Fresno_2 site (36.78, -119.77) that has been operating in the same location since 2012. This site is located about 90 km away from our EM27/SUN measurement site. Further quality control information can be found in Giles et al. (2019).

2.4 Estimating Emission Factors and Modified Combustion Efficiency

185   We demonstrate the capability of ground-based solar column measurements to calculate important variables for fire research including EFs and MCE for determining fire emissions and understanding different combustion phases of wildfires. As a case study, Sept. 12 observations were selected as this day had the highest observed X_{CO} and dominant influence from the SQF Complex (Figure 1b). We estimate emission ratios of CH_4 and CO (ER_i) by calculating the slope from a York linear regression of CO and CH_4 excess mole fractions (ΔX_i) relative to excess mole fraction of (ΔCO_2), as shown in Equation 1. The

190   York linear regression considers the instrument errors in the abscissa and ordinate values.

$$ER_i = \frac{\Delta X_i}{\Delta X_{CO2}} = \frac{X_{i,\ Fire} - X_{i,\ Bkgd}}{X_{CO2,\ Fire} - X_{CO2,\ Bkgd}}. \tag{1}$$

    Emission factors of CH_4 and CO (EF_i) were then calculated as shown in Equation 2 by multiplying the ER_i by the

195   molar mass of either CO or CH_4 (MM_i), divided by the molar mass of carbon (MM_C), and total carbon emitted (C_T) while assuming 500 ± 50 g of carbon is emitted per kilogram of dry biomass consumed ($M_{Biomass}$) (Burling et al., 2010; Akagi et al., 2011). C_T is given by Equation 3, where n is the number of carbon-containing species measured, N_j is the number of carbon atoms in species j, and ΔX_j is the excess mixing ratio of species j (Yokelson et al., 1999).

200    $$EF_i = \frac{ER_i}{C_T} * \frac{MM_i}{MM_C} * M_{Biomass} \tag{2}$$

$$C_T = \sum_{j=1}^{n} N_j \times \frac{\Delta X_j}{\Delta X_{CO2}} \tag{3}$$

The MCE is commonly used as a relative measure between the smoldering and flaming combustion phases. Smoldering emissions have an MCE from 0.65-0.85, pure flaming emissions have an MCE of 0.99 and emissions near 0.9 have roughly

205   equal amounts of flaming and smoldering combustion (Akagi et al., 2011). MCE was calculated by dividing the excess mole fraction of CO_2 by the sum of the excess mole fractions of ΔCO and ΔCO_2:

$$MCE = \frac{\Delta X_{CO2}}{\Delta X_{CO} + \Delta X_{CO2}}. \tag{4}$$

210   Due to averaging kernel differences across the trace gases, an averaging kernel correction is applied to Equations 1 and 4, see Appendix C. The enhancement over background mixing ratios (ΔX_i) for each measurement day was calculated by subtracting the background ($X_{i,\ Bkgd}$) determined as the 2nd percentile of daily measured mixing ratios (X_i). A sensitivity test showed that emission ratios did not change significantly if background was calculated using 1st-5th percentiles. Leveraging the comparison between our ground-based instrument and TROPOMI, we compared the spatial background to show that the

215 2nd percentile was appropriate (Figure S2). The monthly background in September was 411.3 ppm for X_{CO2}, 99.4 ppb for X_{CO} and 1905.3 ppb for X_{CH4}. The monthly average mixing ratios measured *in situ* at Mauna Loa for CO_2 were 411.5 ± 0.2 ppm and CH_4 1884.7 ± 1 ppb during September 2020 (https://gml.noaa.gov/obop/mlo/). Data collected during this period from TCCON sites located in Southern California (CIT and NASA Armstrong) were explored as background sites, however during this period X_{CO} was elevated due to local wildfires in those areas and thus were not appropriate to use during this time.

3 Results

3.1 Observations of X_{CO}, X_{CO2}, X_{CH4}, and AOD from wildfires in the San Joaquin Valley

The first week of trace gas measurements are shown in Figure 2 in addition to the daytime fire radiative power (FRP), an indicator of fire intensity measured by the Visible Infrared Imaging Radiometer Suite (VIIRS) Active Fire and Thermal Anomalies product from NOAA-20. Fire-emitted CO can be observed in the timeseries and X_{CO} is exceptionally high on Sept. 12, reaching mixing ratios ten times higher than the previous days. A regional smoke plume was captured by the NOAA-20 VIIRS satellite on Sept. 12 originating from the SQF Complex and traveling west directly over the measurement site as seen in Figure 1b. Sept. 12 also corresponds to the highest FRP during this record. The next day, Sept. 13, both fires remained active; however, their smoke plumes were transported northward as reflected by a lower X_{CO} in our observations relative to Sept. 12.

X_{CO2} and X_{CH4} were also enhanced on the Sept. 12 smoke event and followed the same trend as X_{CO} over the course of the day. Over 30 dairy farms are located northwest of the measurement site, and they are expected to influence observed X_{CH4} and X_{CO2}; dairy influence is notable on days with predominantly westerly winds (e.g. Sept. 8 and 11). X_{CO}, X_{CO2}, and X_{CH4} averaged at 154 ± 78 ppb, 413 ± 1 ppm, and 1938 ± 27 ppb from Sept. 8 to Oct. 17. X_{CO} and X_{CO2} peaked on Sept. 12 at 1012.8 ppb and 421.6 ppm, while X_{CH4} peaked on Sept. 28 at 2050.1 ppb due to dairy farms in the area. The measured X_{CO} on Sept. 12, is the highest reported X_{CO} value in EM27/SUN literature. Retrievals of X_{gas} using the EM27/SUN in such dense smoke plumes has not been reported in previous studies. Using this date as a case study, we calculate total column EFs and MCE further described in Section 3.4. We isolate the Sept. 12 fire smoke plume by taking the X_{CO} mixing ratios that exceeded the 98th percentile (>335.1 ppb) from all observations over our measurement period. This period corresponded to mixing ratios recorded after 12:00 pm when X_{CO} and X_{CO2} began to increase considerably.

The time since emission of the observed smoke plume was estimated to be ~1.5 hr. This was calculated by dividing the distance away from the SQF Complex fire (~60 km) by the average wind speed (11.2 ± 0.8 m/s) at the height of the smoke plume (4.1 ± 1.2 km). The height of the plume was determined by taking a mean of the available pixels within the smoke plume of aerosol layer height product from TROPOMI (http://www.tropomi.eu/data-products/aerosol-layer-height). The mean wind speed measured at 4.1 ± 1.2 km came from a 915 MHz Wind Profiler located in Visalia, CA about 20 km west of the observational site (data available at: ftp://ftp1.psl.noaa.gov/psd2/data/realtime/Radar915/).
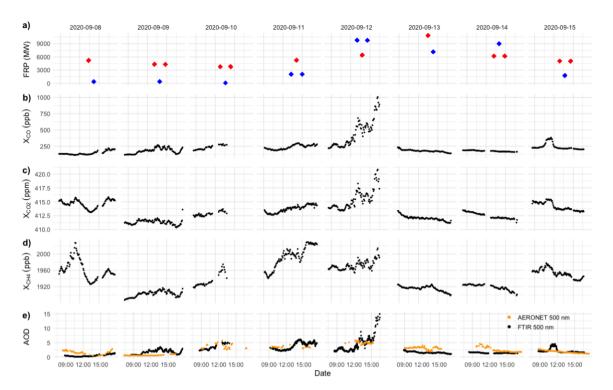
Figure 2. Timeseries during the first week of measurements Sept. 8 – 15, 2020. a) Daytime total FRP from VIIRS NOAA-20 of Creek Fire (red) and SQF Complex (blue). b-d) 5-minute mean observations from the ground-based EM27/SUN solar-viewing spectrometer of X_{CO}, X_{CO2} and X_{CH4}. e) FTIR-derived AOD (black) and AERONET AOD at 500 nm (orange).

We show a timeseries of AOD at 500 nm derived for the first week of measurements in Figure 2, panel e (Sept. 8 – 15) plotted with AOD at 500 nm from an AERONET station in Fresno, located about 90 km north of the measurement site (Figure 1). Similar to observations of X_{CO}, enhancements of AOD are observed throughout the week with the highest recorded AOD on Sept. 12. The observational sites were relatively far from each other (~90 km) and although smoke reaching the two sites varied over these spatial scales, the FTIR AOD follows the same interday trend as the AOD measured by the AERONET with a peak in AOD on the Sept. 12. Intraday variability between the sites do not seem to follow the same trend. This suggests that the EM27/SUN AOD estimate was also able to qualitatively capture the increase in aerosols in the SJV as fires burned more intensely and smoke from fires moved into the valley due to synoptic conditions. A comparison between the FTIR and AERONET hourly AOD can be found in the supplements Figure S3, where we find a slope of 1.4 ± 0.3 and R^2 of 0.39. Differences are observed in the AOD timeseries as these two sites were downwind of two different fires in the Sierra Nevada: the Creek Fire was located directly east of Fresno and the SQF Complex was located directly east of the EM27/SUN measurement site. This may be the reason why the peaks observed at the FTIR site are not seen in the Fresno AERONET data. Ahangar et al. (2022) determined that the SJV air quality was mainly impacted during the Sept. 8 – 15 period with Creek and SQF Complex fires responsible for the majority of the smoke within SJV. Although the Creek Fire began on Sept. 5, the air

9

quality began to deteriorate a few days after, possibly due to the westerly downslope winds that pushed the smoke east of the Sierra Nevada at the beginning of the fire (Cho et al., 2022). Low AOD from AERONET was observed prior to Sept. 8 with values of 0.50 ± 0.28, illustrating the air quality was cleaner and deteriorated after the activity from the Creek and SQF Complex fires increased (Ahangar et al., 2022).

270   Figure 3 shows vertical column X_{CO} plotted against simultaneously collected AOD at 500 nm for 1-minute intervals. The points are colored to distinguish the different measurement days from Sept. 8 to Sept. 15. The error bars are the uncertainty in AOD that is further described in Appendix B and for X_{CO} it is one standard deviation on the mean. Due to rapidly changing X_{CO} as the fire plume traversed over the instrument, we use the standard deviation from 1-minute X_{CO} mean as the natural variability or uncertainty, which is larger than the X_{CO} instrument error. Table 1 shows the slope and intercepts with standard

275 errors from a York linear regression fit that considers errors in x and y. We find strong relationships ($R^2 > 0.61$) between the EM27/SUN X_{CO} and AOD at 500 nm with slopes ranging from 29.01 to 92.41 ppb X_{CO}/AOD (Table 1 and Figure 3). Several studies have also found strong correlation between CO and AOD at 500 and 550 nm from fire events and downwind of polluted sources (Lobert, 2002; Paton-Walsh et al., 2005; Kampe and Sokolik, 2007; McMillan et al., 2008). McMillan et al. (2008) found mean slopes of fire plume observations from AIRS CO and MODIS AOD that ranged from 40 to 74 ppb/AOD and over

280 clean regions slopes averaged at 35 ppb/AOD. Most of the days from our observations have slopes that fall within these ranges and the days with lower slopes (Sept. 10 and 11) follow a similar linear trend (grey line in Figure 3) as in McMillan et al. (2008) over a clean region in Alaska and Canada. Kampe et al. (2007) found that AOD/CO slopes varied strongly, and this variation may depend on age of smoke plume, distance from source, combustion efficiency, and local meteorological factors. Our measurements were sensitive to nearby smoke plumes as well as mixed smoke from distant fires. The intercepts of the

285 fitted lines reflect different local backgrounds of CO during measurement periods with Sept. 10 – 12 having the largest backgrounds of X_{CO}. We find that the AOD on Sept. 12 reached values above 15 indicating extremely high aerosol loading from the smoke plume event transported from the SQF Complex in the Sierra Nevada.

Table 1. Summary of York linear fit of X_{CO} and AOD for Sept. 8 – 15, 2020.

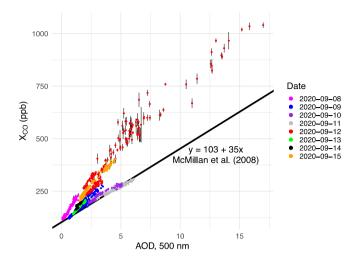| Measurement date	Slope (ppb X_{CO}/AOD)	Intercept (ppb)	R^2
2020-09-08	81.8 ± 0.2	109.89 ± 0.08	0.97
2020-09-09	55.57 ± 0.07	87.47 ± 0.09	0.94
2020-09-10	33.84 ± 0.04	116.3 ± 0.1	0.94
2020-09-11	29.01 ± 0.02	128.60 ± 0.07	0.98
2020-09-12	62.42 ± 0.07	114.5 ± 0.2	0.94
2020-09-13	57.55 ± 0.04	90.94 ± 0.06	0.87
2020-09-14	92.41 ± 0.06	50.72 ± 0.08	0.61
2020-09-15	72.87 ± 0.04	95.60 ± 0.08	0.98

290

Figure 3. Scatterplot correlations of X_{CO} and AOD at 500 nm from the FTIR for each day from Sept. 8 – 15, 2020. Some days fall along the grey line that was derived from previous remotely sensed X_{CO}/AOD relationships over a clean region. The red markers correspond to Sept. 12, the day of highest fire influence in our record.

3.2 Comparison of EM27/SUN and TROPOMI retrievals

In this section, we compare X_{CO} retrieved from ground-based EM27/SUN observations downwind of the Sierra Nevada wildfires to satellite-based X_{CO} retrievals from coincident TROPOMI overpasses. Previous studies of X_{CO} and X_{CH4} comparisons between TROPOMI and EM27/SUN have used TROPOMI soundings between 50 – 100 km from the observational site and used EM27/SUN measurements between 40 mins – 1 hour of the TROPOMI overpass as a coincident criteria (Jacobs, 2021; Sha et al., 2021; Alberti et al., 2022b; Sagar et al., 2022). Given the spatial and temporal heterogeneity in smoke plumes from wildfires observed in Figure 1 and Figure 2, we perform a sensitivity study of different radii (10, 15, 20, 30, 40, 50 km) from our observational site and time averages (10, 15, 20, 30 mins) to determine adequate criteria for comparison during a wildfire event. An illustration of the sensitivity analysis is shown in Figure D1, Appendix D.

We quantify the sensitivity of different TROPOMI radii and averaging times in comparison with our EM27/SUN observations by calculating the mean difference, mean relative difference and R^2 between the linear regression fits for the measurements. We find that all combinations produce a positive mean bias, meaning that TROPOMI overestimates X_{CO} compared to the EM27/SUN measurements. TROPOMI pixels within a radius of 5 km averaged with 30-minute aggregations of EM27/SUN gives the lowest mean difference of 10.64 ppb, mean relative difference of 5.5%, and highest correlation coefficient of 0.99, however, only 4 points coincide during the measurement period. To maximize the number of coincidences while maintaining a low bias, we select 15 km as the maximum radius with a 30-minute averaging time. This gives a total of 19 coincident data points and mean difference of 17.2 ppb, mean relative difference of $9.7 \pm 1.3\%$, and R^2 of 0.97. A timeseries of the coinciding data pairs from the EM27/SUN 30-minute average observation period with TROPOMI overpass with 15 km radii are shown in Figure 4a and the comparison is shown in Figure 4b. Applying these spatial and temporal criteria results in

11

large variance for the largest measured X_{CO} due to heterogeneity in the smoke plume event. The EM27/SUN displays a larger variance than TROPOMI due to capturing the 30-minute temporal variability in the plume as it was transported above the instrument. We find a strong correlation between X_{CO} column averages with an R^2 of 0.97 and a York linear regression fit of y = (1.35 ± 0.01) x − 39.30 ± 0.58. The mean relative difference found in this study of 9.7 ± 1.3% is similar to the systemic difference of 9.22 ± 3.45% between TROPOMI and all TCCON stations (Sha et al., 2021). These results suggest the difference found between TROPOMI and EM27/SUN observations during wildfires are consistent with systematic differences that exist between the two instruments, however based on our sensitivity study, biases may exist based on sampling conditions in a spatially and temporally heterogenous source.
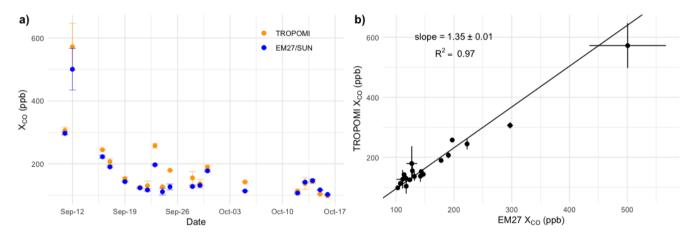
Figure 4. a) Timeseries of coinciding EM27/SUN 30-minute average observation period with TROPOMI overpass with 15 km radius. b) Correlation between coinciding TROPOMI and EM27/SUN data pairs. The error bars are the standard deviation of the TROPOMI averaged pixels at 15 km and EM27/SUN 30-minute observation.

3.3 Emissions factors and modified combustion efficiency

Emission ratios of CO and CH_4 on Sept. 12 were calculated with respect to CO_2 (Figure 5). ER_{CO} was 0.1161 ± 0.0005 and the ER_{CH4} was 0.00730 ± 0.00007, resulting in an EF_{CO2} of 1632.9 ± 163.3 g CO_2 per kg biomass combusted, EF_{CO} of 120.5 ± 12.2 g CO per kg biomass combusted, and a EF_{CH4} of 4.3 ± 0.8 g CH_4 per kg biomass combusted. We compared findings from our measurements to literature values in temperate coniferous forest studies from the Sierra Nevada (Figure 6) and other locations in North America summarized in Table 2. All the studies listed in Table 2 except for this study were based on aircraft measurements for temperate coniferous forests. Due to combustion phase variability in field studies, we compare our atmospheric column-based EFs in Figure 6 with the most relevant studies from the Sierra Nevada, which shows our calculated values within the expected linear range as *in situ* aircraft studies. The measurement uncertainties for the EFs were calculated by propagating the error from the ER linear regression standard error, C_T, and 10% error from $M_{Biomass}$.

The average MCE for the smoke plume on Sept. 12 was 0.89 ± 0.21 (1σ), meaning that observations of the smoke plume consisted of a mixture of flaming and smoldering combustion phases (Figure 6). During the flaming phase of a fire, CO_2 is produced, and convection is created by high flame temperatures and produces lofting of smoke. High altitude smoke can be transported large distances, corroborated by observations of ash falling from the sky at the measurement site ~60 km away from the fire and clearly observable by satellite imagery (Figure 1b). In contrast to the flaming phase, smoldering fires burn at lower intensity, and incomplete combustion side products like CO, CH_4, and organic carbon aerosol are produced. The MCE calculated from total column observations is averaged over the entire vertical plume as it was being transported over the measurement site. The advantage of a plume integrated MCE is that vegetation is burnt differently throughout the fire and the atmospheric column observations can represent the fire as a whole by integrating the smoke plume heterogeneity in the vertical atmospheric column.
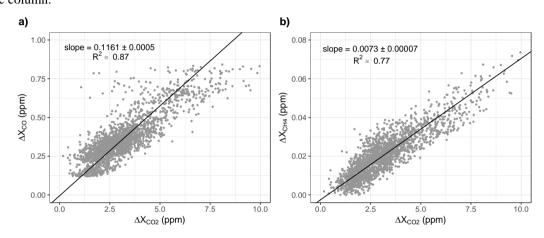

Figure 5. Relationship between a) ΔCO and b) ΔCH_4 against ΔCO_2 during the SQF Complex wildfire plume on Sept. 12, 2020.
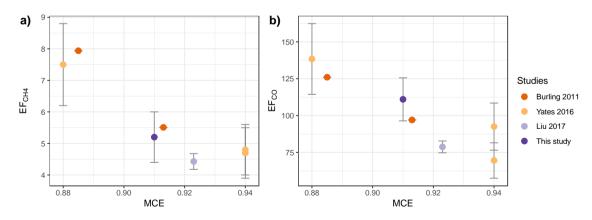

Figure 6. Emission factors (g kg^{-1}) for a) CH_4 and b) CO as a function of MCE for temperate coniferous forests in Sierra Nevada wildfires.

Table 2. Summary from past airborne studies and the present study of modified combustion efficiency (MCE) and emission factors (EF, g kg^{-1}) of CO and CH$_4$ relative to CO$_2$ for temperate coniferous forests in North America and the Sierra Nevada.

Studies	MCE	EF$_{CO_2}$	EF$_{CO}$	EF$_{CH_4}$
North America				
Radke et al., 1991* – Conifer Forest	0.919	1641	93	3.03
Yokelson et al., 1999* – Southeastern US Pine Forest understory	0.926	1677	86	-
Yokelson et al., 2011 – Mexico Pine-oak	0.908	1603	103	3.66
Burling et al., 2011* –Average conifer forests understory burns	0.936 ± 0.024	1668 ± 72	72 ± 26	3.0 ± 2.4
Urbanski et al., 2013 – Rocky Mts conifer forest fires	0.85 – 0.92	1527 – 1681	89.3 – 173	4.4 – 12.1
Liu et al., 2017 – Study average	0.912	1454 ± 78	89.3 ± 28.5	4.9 ± 1.5
Sierra Nevada				
Burling et al., 2011				
Turtle Fire* (10-Nov-2009)	0.91	1599	97	5.51
Shaver Fire* (10-Nov-2009)	0.885	1523	126	7.94
Yates et al., 2016				
Rim fire (26-Aug-2013)	0.94	1675 ± 285	92.5 ± 16	4.8 ± 0.8
Rim fire (29-Aug-2013)	0.94	1711 ± 292	69.5 ± 12	4.7 ± 0.8
Rim fire (10-Sept-2013)	0.88	1595 ± 272	138.4 ± 24	7.5 ± 1.3
Liu et al., 2017				
Rim fire (26-Aug-2013)	0.923	1478 ± 11	78.7 ± 4	4.43 ± 0.25
This study: SQF Complex fire (12-Sept-2020)	**0.89 ± 0.21**	**1632.9 ± 163.3**	**120.5 ± 12.2**	**4.3 ± 0.8**

*Prescribed burns

3.4 Enhancement ratios of livestock and wildfire emissions

The EM27/SUN's location enabled us to sample transient fire plumes from local and state wildfires, but was also located near a large cluster of dairy farms, which are a large regional source of CH$_4$ emissions (Heerah et al., 2021; Marklein et al., 2021). Dairy farms are known to emit significant amounts of CH$_4$ from the animal's enteric fermentation and on-farm manure management. Because fires also emit CH$_4$, we explored whether dairy and fire sources in this region can be disentangled using enhancement ratios of the different species measured by the EM27/SUN. Enhancement ratios are also known as the normalized excess mixing ratios. Excess mixing ratios are calculated by subtracting the mixing ratio of a species from a source plume minus a mixing ratio of the same species in background air. To correct for dilution, excess mixing ratios are normalized by a stable tracer such as CO$_2$. When an enhancement ratio does not change with dilution and mixing with

14

background air, the enhancement ratio is equal to the emission ratio (ER) of a source (Yokelson et al., 2013). Furthermore, our measured $\Delta X_{CH4}/\Delta X_{CO2}$ ratios enable us to investigate the contribution of state wildfires to CH_4 emissions in 2020. To constrain

370 the observed enhancements, we compared the enhancement ratios of $\Delta X_{CH4}/\Delta X_{CO2}$ from September – October 2020 to enhancement ratios collected in September 2018 and 2019 in the same local area that characterize non-fire years. September 2018 and 2019 measurements are further described in the supplemental information. We focused on observation days with statistically significant correlations (n = 26 days) between CH_4 and CO_2 enhancements ($R^2 > 0.5$ and $p < 0.05$) to characterize enhancement ratios of the SJV non-fire years.

375   During Sept. – Oct. 2020 observations, $\Delta X_{CH4}/\Delta X_{CO2}$ ratios of dairy farm influence were found on several days in addition to lower slopes indicative of combustion sources (Figure 7, grey markers). The Sept. 12 smoke plume event is highlighted in Figure 7 (red markers) and has a smaller emission ratio of 7.3 ± 0.07 (ppb/ppm) compared to larger $\Delta X_{CH4}/\Delta X_{CO2}$ enhancement ratios of 38.4 ± 21.7 and 30.5 ± 5.0 (ppb/ppm) observed in Sept. 2018 and 2019. Similar non-wildfire ratios of $\Delta X_{CH4}/\Delta X_{CO2}$ were found in Hanford, ~40 km west of our observation site, from an aircraft study ranging from 35.9 – 44.4

380 (ppb/ppm) during a winter campaign (Herrera et al., 2021). Other column-based studies have determined the X_{CH4}/X_{CO2} for urban sources in the Los Angeles City finding ratios ranging from 6.65 to 9.96 (ppb/ppm) in 2015 (Chen et al., 2016) and 11 ± 2 per mil in 2008 (Wunch et al., 2009). Wunch et al. (2009) determined that urban fossil fuel and wildfire X_{CH4}/X_{CO2} ratios are very similar due to incomplete combustion and ratios are not distinct enough to separate. In the vicinity of the measurement site in the SJV, there is a strong influence of dairy farm agriculture and minimal urban emissions away from population centers,

385 thus we are able to separate of $\Delta X_{CH4}/\Delta X_{CO2}$ from dairy sources, from fire or possible urban emissions. The CH_4/CO_2 enhancement ratios observed in this area make it evident that dairy farms operations are the dominant source of CH_4 during fire and non-fire days. Nevertheless, CH_4 enhancements during the strong smoke events greatly exceeded CH_4 enhancements from local dairy sources on hourly time scales.
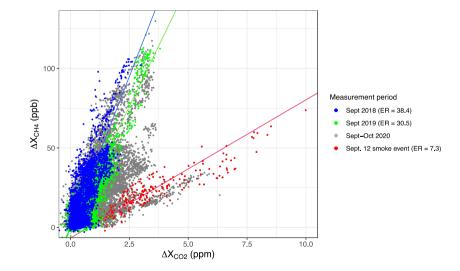

390

Figure 7. Correlation plots of ΔX_{CH4} vs ΔX_{CO2} for SJV measurements collected during non-fire years in Sept. 2018 (blue) and 2019 (green), and during the fire period of Sept. – Oct. 2020 (gray). The Sept. 12, 2020, smoke event (red) highlighted with a linear fit through the day's data clearly shows a distinct $\Delta X_{CH4}/\Delta X_{CO2}$ relationship.

3.5 Total methane emissions from wildfires in California

The immense scale of the 2020 wildfires released a significant amount of CO_2 emissions, equivalent to about 36% of the state's CO_2 budget for the year (CARB, 2022a). Our observations of X_{CH4} suggest that the wildfires may have also had a significant effect on the state's CH_4 budget. Given the importance of reducing CH_4 emissions for meeting California's climate goals, we calculate the amount of CH_4 released from wildfires that burnt in the state in 2020 by using estimates of CO_2 emissions from the state's wildfire inventory and ER_{CH4} calculated from our study as well as from literature values.

The California Air Resources Board (CARB) reported that a total of 106.7 Tg of CO_2 was emitted from 2020 wildfires and reported individual CO_2 emission estimates for the 20 largest wildfires of 2020. Using the reported CO_2 emission estimates from individual wildfires, we derived CH_4 emissions by multiplying the CO_2 estimates with emission ratios of CH_4 (ER_{CH4}) from wildfire smoke and molecular mass ratios:

$$E_{CH4} = \left(ER_{CH4} \times \frac{M_{CH4}}{M_{CO2}} \right) E_{CO2} \tag{5}$$

where E_{CH4} is the emissions of CH_4 in Gg/yr, ER_{CH4} is the emission ratio of CH_4 with respect to CO_2 in mol/mol, M_{CH4} is the molar mass of CH_4, M_{CO2} is the molar mass of CO_2, and E_{CO2} are the individual wildfire emissions of CO_2 in Gg/yr. Emission ratios from fires are dependent on vegetation type; fires in California fell into temperate forest, shrubland or grassland vegetation types (Xu et al., 2022). Based on the generic vegetation classification from the Fire INventory from NCAR (FINN) model (https://www.acom.ucar.edu/Data/fire/), we classify the top 20 California wildfires of 2020 into the three types based on the dominant vegetation: temperate forest, shrublands, or grasslands. We assign an ER_{CH4} for each general vegetation type based on the mean EF_{CH4} found in Xu et al. (2022) that summarized EFs from Prichard et al. (2020). The standard deviation of the EF_{CH4} was calculated based on Pritchard et al. (2020) and taken as the uncertainty that was then propagated in the ER_{CH4} calculations. For the Sierra Nevada wildfires (Creek Fire, SQF Complex, and North Complex), we derive a ER_{CH4_avg} by first calculating an average EF_{CH4_avg} from Sierra Nevada specific EF_{CH4} in Table 1 ($EF_{CH4\_avg} = 5.6 \pm 1.5$ g kg^{-1}). We then used Equation 2 to solve for ER_{CH4} with C_T equal to 1 ($ER_{CH4\_avg} = 0.0084 \pm 0.0022$). A summary of ER_{CH4} can be found in Table E1, Appendix E. Methane emissions for the top 20 wildfires were then calculated using Equation 5 with CARB's CO_2 estimate from each individual fire and summed to obtain a total CH_4 emitted from these reported wildfires. Figure 8 shows the estimated CH_4 emissions from the top 20 wildfires of 2020 compared to CARB's 2020 anthropogenic CH_4 inventory emissions (CARB, 2022b). The error bar from this estimate was calculated by propagating the general vegetation ER_{CH4} error from Table E1 into each individual wildfire CH_4 estimate and added in quadrature to obtain a total error. The 20 largest wildfires of 2020 emitted

92% of total CO_2 emissions released from wildfires in that year and emitted 213.7 ± 49.8 Gg CH_4 or 13.7% of total anthropogenic CH_4 emissions.
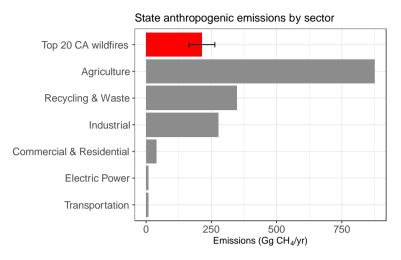

Figure 8. California CH_4 emissions from 2020 calculated for the top 20 wildfires of 2020 compared to the state's anthropogenic CH_4 emissions from the 2020 inventory (CARB, 2022b). The industrial sector also includes oil and gas emissions.

4. Discussion

We demonstrate EM27/SUN total column measurements can be used for calculating MCE and EFs in smoke plumes transported from wildfires, especially for high altitude smoke, adding important new estimates for fires in this region. For the Sierra Nevada, only three field-based studies have estimated emission factors in this area despite the increase in wildfires burns over the previous decade (Burling et al., 2011; Yates et al., 2016; Liu et al., 2017). Table 1 highlights the variety of EFs and MCE sampled over the Sierra Nevada and North America. Despite the variability, our emission factor estimates from the Sept. 12 event for CO_2 (1632.9 ± 163.3 g kg^{-1}), CO (120.5 ± 12.2 g kg^{-1}) and CH_4 (4.3 ± 0.8 g kg^{-1}) are within the range of those reported from the Sierra Nevada conifer forests. Additionally, our calculated emission factors also agree well with recently compiled emission factors for North American conifer forests, where Prichard et al. (2020) found a fire average for EF_{CO2} of 1629.54 ± 63.43, EF_{CO} of 104.01 ± 34.93, and EF_{CH4} of 5.05 ± 2.41. Methane emission ratios reported for smoldering fires that were characterized by direct O_2/CO measurements for California 1999 Big Bar Fire are also consistent with our measurements (Lueker et al., 2001). These atmospheric column-based estimates contribute to the limited number of EFs for temperate forests and are particularly important given the scale of the fires that occurred in 2020 in California. Empirically quantified EFs in temperate conifer forests are limited in number and many of the measurements in these regions are from prescribed burning for land management (Burling et al., 2011; Akagi et al., 2011; Urbanski, 2013). Because prescribed burns typically occur during favorable atmospheric conditions, specified fuel, and during non-wildfire seasons, it is possible that prescribed burn EFs may not represent wildfire EFs that burn under different conditions favorable to wildfires (Urbanski, 2013). There is a

need for biome-specific EFs to quantify the amount of trace gas or aerosol emitted per kilogram of biomass burned, and these

450   EFs are essential model inputs for estimating total greenhouse gas and aerosol emissions of fires.

        While advantages of this technique allow for understanding regional scale emissions, limitations exist with this method. The EM27/SUN solar column observations are limited to daytime hours as the instrument requires the sun as the light source. For this reason, we were not able to capture nighttime observations despite the continued release of smoke emissions and growing concern of increasing nighttime wildfire activity in the continental U.S. (Freeborn et al., 2022). Additionally,

455   optically thick smoke plumes obstruct the sunlight and prohibits continued measurements when the solar disk is not traceable by the instrument's solar tracker. Exposing the instrument's mirrors to harsh conditions such as ash decreases the instrument signal and may decrease the lifetime of mirrors. Although total column measurements are sensitive to larger scales than *in situ* stations, the FTIR is limited to the line of sight of the instrument and on occasions can miss the plume like we did on Sept. 13 and 14. Whereas aircraft observations have extensive spatial reach and more flexibility in locating and sampling plumes to

460   obtain spatially rich information of the plume. However, when used in tandem with satellite observations our instrument collects continued temporal observations of a site of interest that a satellite does not, thus synchronous observations provide a better spatiotemporal understanding of the emission source. EM27/SUN instruments are also costly which can limit the number of instruments deployed. Unless instruments are secured properly as it has been done in long term FTIR network studies (Frey et al., 2019; Dietrich et al., 2021), measurements require personnel to set up and operate the instrument daily. The EFs, MCE,

465   and their uncertainties fall within the range of expected values, thus lends confidence that this technique can be used for studying combustion phases of wildfires for other vegetation types. Despite the limitations of the EM27/SUN, we demonstrate the ability to gather new information of EFs, MCE and AOD for understudied vegetation types and regions. Furthermore, the EM27/SUN observations can be used as a validation tool for orbiting satellites like TROPOMI, Orbiting Carbon Observatory-2 (OCO-2), OCO-3, and future satellites. The next generation weather forecasting, greenhouse gas, and air pollutant satellites

470   such as Tropospheric Emissions: Monitoring of Pollution (TEMPO) will have more temporal frequency and greater spatial resolution allowing for continuous monitoring of burning activity and smoke emissions (Zoogman et al., 2017). This may allow remote sensing products to provide new insight into fuel properties of many types of vegetation in remote areas. It will also be important to evaluate satellite-based observations with ground-based stations like the EM27/SUN, as we did in this study.

475   Simultaneous measurements of ground-based total columns and satellites allow for a spatial and temporal understanding of the fire events. The X_{CO} enhancement from the 2020 wildfires in the Sierra Nevada was also observed from space and in concentrated smoke plumes X_{CO} was up to ten times higher than the local background, which was clearly visible in the TROPOMI soundings during the Sept. 12 smoke plume event. Pairing stationary ground-based column observations with satellites can help in understanding regional wildfires at a greater spatial and temporal scale. Although TROPOMI has

480   daily global coverage with high spatial resolution, daily snapshots are often not enough to understand the behavior of a fire. Conversely, stationary ground-based instruments are limited to observing a line of sight or point in space. As an instrument with capability of measuring atmospheric columns, the EM27/SUN can help close the gap in the temporal scale of satellite

observations. The EM27/SUN measured continuously in the daytime filling in the temporal gaps from the satellite TROPOMI's single overpass observations. A sensitivity study showed that a smaller radius of 5 or 15 km from TROPOMI observations paired with 30-minute averaging around the overpass time gave better statistical agreement during wildfire events. This strong correlation of X_{CO} between TROPOMI and the EM27/SUN has been observed before in urban sites (Sagar et al., 2022; Alberti et al., 2022b) and in rural Alaska (Jacobs, 2021). Jacobs (2021) found that wildfire influences in X_{CO} resulted in high observational variance in EM27/SUN observations and suggest that this may be due to spatial and temporal variability in the smoke plume measured by TROPOMI and the EM27/SUN. The 9.7 ± 1.3% mean relative difference between the EM27/SUN and TROPOMI found in this study may also be due to averaging of the smoke plume's heterogeneity within each TROPOMI comparison point. Alternatively, Rowe et al. (2022) found that multiple scattering on aerosols may be responsible for 5-10% of the increased X_{CO} observations from TROPOMI in thick smoke plumes.

The air quality index in the SJV was at an all-time high in the hazardous range for weeks during the 2020 wildfire season (Morris III and Dennis, 2020) and AOD at the AERONET site in Fresno increased by three to five times higher than yearly average from 2002-2019 (Cho et al., 2022). FTIR-derived AOD at 500 nm reached extreme highs during the Sept. 12 smoke plume event, and followed the same trend on other days as the trace gas enhancements. The slopes during low smoke and high smoke days were consistent with previous satellite observations by McMillan et al. (2008). Previously, simultaneous measurements of aerosols and trace gases from the same instrument has been limited due to the aerosol burden interfering with retrieval of trace gases. For example, the majority of the TROPOMI X_{CH_4} product was flagged out completely near the observational site during the Sept. 7 – 15 period, and hence was not included in this analysis. The EM27/SUN demonstrated the potential to elucidate trace gas and aerosol relationships even during thick aerosol periods. Similarly, future studies may use simultaneous measurements from TROPOMI X_{CO} product and AOD to study regional impacts from wildfires (Chen et al., 2021). Scattered diffuse light during high aerosol loading from biomass burning may decrease the reliability of the AOD observations, thus further verification of the FTIR-derived AOD during high aerosol loading is required. Since the nearest AERONET station was relatively far away from our EM27/SUN site, we cannot do a true side-by-side comparison. However, the FTIR-derived AOD showed the same baseline pattern as the AERONET site in Fresno, demonstrating the ability of the EM27/SUN to simultaneously measure AOD and trace gases through a thick plume of smoke which can elucidate mechanisms within smoke plumes.

Estimates of CH_4 emitted from biomass burning are commonly calculated for global inventories such as FINN, Global Fire Emissions Database (GFED), and Intergovernmental Panel on Climate Change (IPCC) guidelines that rely on satellite observations of area burnt and observation-based emission factors (Wiedinmyer et al., 2011; van der Werf et al., 2017), however these bottom-up CH_4 inventories tend to report large uncertainties (Saunois et al., 2020). In California, statewide wildfire estimates of CO_2 and PM are based on the US Forest Service's First Effects Model (FOFEM) (Reinhardt and Dickinson, 2010), though reporting of CH_4 estimates from wildfires are lacking despite the importance of CH_4 for meeting the state's ambitious climate goals. To reduce uncertainties and constrain emissions of global and local CH_4 budgets, more atmospheric based estimates of CH_4 emissions are required as currently few observation-based studies exist that focus on

estimating CH_4 emissions (e.g., Mühle et al., 2007 and Worden et al., 2013). As wildfires become more frequent with climate change, monitoring trace gases and particulates may become especially challenging in mixed source areas like the San Joaquin Valley where concentrations can become amplified by stagnant atmospheric conditions. Moreover, the fire-added CH_4 may hamper evaluation of greenhouse gas emission reduction initiatives at the state and at the global scale by adding unaccounted CH_4 to the atmosphere. Using CARB's 2020 wildfire emission estimate for CO_2, we calculated the CH_4 contribution from the 20 largest fires to be 213.7 ± 49.8 Gg CH_4. These wildfires alone emitted 13.7% of the total state anthropogenic CH_4 emissions, more than the commercial and residential, transportation, and electric power sectors. While estimated CH_4 emissions from wildfires are smaller in magnitude than inventoried emissions from agriculture, waste, and industrial sources, this source should be accounted for in the state's greenhouse gas inventories given its magnitude and large impacts on the atmospheric CH_4 during wildfire periods. Globally, about 10% of anthropogenic global CH_4 is emitted by biomass burning (Saunois et al., 2020) and may be an important and unaccounted positive feedback to climate change given the effect of increasing temperatures on fire severity.

5. Conclusions

Over the past 50 years, approximately three quarters of the area burned by wildfires in California has been in the Sierra Nevada and North Coast, highlighting the importance of studying emission factors from fires in these ecosystems. However, there are surprisingly few observations of emission factors from these fires despite their importance to California's greenhouse gas budget and air quality implications. The ground-based EM27/SUN is a useful instrument for understanding emissions of trace gases and aerosols from wildfires at regional scales. The portable nature of the EM27/SUN allows for deployment downwind of fires and for calculating important variables like EFs and MCE. Having alternative techniques to observe emissions of wildfires can help add to the limited number of emission factors for understudied vegetation and improve emissions estimates of biomass burning. Several studies have demonstrated the utility in FTIR-derived EFs for studying whole fire emissions from open-path instruments and vertically integrated measurements. Our total column MCE and EF with respect to CO_2 are the first to be reported from ground-based FTIR measurements in California.

Wildfire smoke produced overcast skies throughout the Western U.S. during this period, with smoke plumes transported long distances. The EM27/SUN measures a vertically integrated regional signal but is limited spatially compared to observations from satellites. Here we show that a combination of the two can elucidate spatiotemporal variability of wildfire emissions. We find strong agreement between the EM27/SUN and TROPOMI with a mean relative difference of $9.7 \pm 1.3\%$ between the platforms. This is consistent with systematic differences between TCCON and TROPOMI as well as with previous studies of EM27/SUN X_{CO} in rural Alaska and Idaho wildfires. Additionally, our solar spectral measurements at 1020.9 nm were used to derive AOD at 500 nm to compare to a nearby AERONET site and compare AOD to CO ratios with previous studies. We found that our AOD values followed the same intraday pattern as the AERONET observations. AOD at 500 nm reached extreme levels of up to 15 during the smoke plume event. Good agreements were found of AOD to CO ratios with those observed over the U.S. and Canada from MODIS AOD and AIRS CO.

Finally, we find that a significant amount of CH_4 was emitted from the largest 20 wildfires of 2020 in California. Given the importance of CH_4 emissions reduction for the state, our study suggests wildfires are an important source of CH_4 for California and may delay meeting the state's ambitious goals of reducing greenhouse gas emissions. Atmospheric CH_4 emissions released during wildfire periods should also be accounted for in statewide greenhouse gas inventories, as wildfire

555   CH_4 enhancements are clearly measurable, and their yearly emissions are comparable or larger than other CH_4 sectors. Overall, our analysis contributes to the development of techniques for analyzing remotely sensed greenhouse gases and aerosol measurements from wildfires.

560

Appendix A: EM27/SUN Correction Factors

The EM27/SUN was co-located with the CIT TCCON for 2 – 3 days before (Sept. 2 and 3, 2020) and after (Oct. 30, 31 and Nov. 31, 2020) the field measurements. A summary of the correction factors is shown in Table A1. An averaging kernel correction has been applied to the EM27/SUN observations prior to comparison following Hedelius et al. (2016). Due to a camera misalignment on Sept. 2 and 3, X_{CO} correction factors for those dates are not reported.

Table A1. Summary of correction factors from co-located EM27/SUN measurements with TCCON at CIT.

X_{gas}	Sept 2 & 3	Oct 30, 31 & Nov 1
X_{CH4}	0.9986 (0.0002)	0.9976 (0.0001)
X_{CO2}	1.0042 (0.0001)	1.0036 (0.0001)
X_{CO}	-	0.9737 (0.0028)
X_{H2O}	1.0044 (0.0005)	1.0101 (0.0005)

Appendix B: Aerosol Optical Depth Calculation

To calculate AOD from the EM27/SUN solar measurements, we follow the methods described in Barreto et al. (2020) who found good agreement between AERONET and TCCON FTIR-derived AOD at the high altitude Izaña Observatory in Spain. Their analysis was performed on degraded TCCON FTIR solar spectra (0.5 cm^{-1}) to assess the capability of lower resolution FTIR EM27/SUN instruments to detect broadband aerosol signal. Ten interferogram scans were co-added to increase the signal to noise ratio of the aerosol retrieval for a total integration time of 1 minute. The uncertainty in the AOD product in this study is determined by adding in quadrature the estimated uncertainty of ~0.006 determined in Barreto et al. (2020) for the 10 co-added interferogram scans for a total uncertainty of 0.02 for a 1-minute analysis. We calculated AOD from four recommended micro-windows with high solar transmission centered at 1020.9, 1238.25, 1558.25, and 1636 nm and compare to a nearby AERONET site located in Fresno, CA.

We apply the methods further described in Barreto et al. (2020) that are based on the Beer-Lambert-Bougher attenuation law:

$$V_\lambda = V_{o,\lambda} \cdot d^{-2} \cdot \exp\left(-m \cdot \tau_\lambda\right) \tag{B1}$$

where V_λ is the measured solar irradiance at wavelength λ, $V_{o,\lambda}$ is the spectral irradiance outside the Earth's atmosphere at wavelength λ, d is the ratio of mean to actual sun-earth distance, and m is the optical air mass (Kasten and Young 1989). The V_o is derived from the Langley method by utilizing the measured solar intensity (V) versus the optical air mass (m) and

extrapolating to an optical air mass of zero. The total optical depth (τ_λ) is the sum of the optical depth of Rayleigh scattering ($\tau_{R,\lambda}$), gas absorption ($\tau_{g,\lambda}$), and aerosols ($\tau_{a,\lambda}$):

590

$$\tau_\lambda = \tau_{R,\lambda} + \tau_{g,\lambda} + \tau_{a,\lambda}. \tag{B2}$$

Barreto et al. (2020) carefully selected and evaluated several FTIR micro-windows to minimize the gas absorption, thus $\tau_{g,\lambda}$ is considered negligible. Rayleigh scattering is calculated following Bodhaine et al. (1999) using the pressure measured at the
595 measurement site by the ZENO weather station. The AOD $\tau_{a,\lambda}$ can then be calculated by subtracting Rayleigh scattering from the equation below:

$$\tau_{a,\lambda} = \frac{\ln(V_{o,\lambda} \cdot d^{-2} \cdot) - \ln(V_\lambda)}{m} - \tau_{R,\lambda} . \tag{B3}$$

600   A cloud filter is applied to the spectra based on the measured fractional variation in solar intensity (fvsi). We set this quality filter to a maximum of 0.5% variability to ensure minimum cloud interference. The optical air mass range for Langley plot calibrations were performed from $1.5 \leq m < 7$ to avoid large errors at smaller air masses and turbidity influence at solar noon. A plot of ln(Vo) is found in Figure B1 displaying the calculated ln(Vo) over time from September to November 2020. Mirror degradation and exposure to dust or ash from fires can be observed in a declining ln(Vo) and a sudden jump in ln(Vo)
605 is observed in late October and early November after the mirrors were cleaned, suggesting that debris had diminished the solar intensity measured by the FTIR instrument. Due to the varying ln(Vo), we calculate AOD only for the first week of data collection (Sept. 8 – 15) using the ln(Vo) obtained during the earlier period of September, summarized in Table B1.

      A time series of the FTIR-derived AOD for the four micro windows is shown in Figure B2 where a spectral dependance of the aerosol absorption can be observed in the plot with longer wavelengths recording smaller AOD. Although
610 our FTIR-derived AOD is limited to the spectral range from the FTIR detector (1020.9 – 1636 nm), we used the Ångström exponent to derive FTIR AOD at 500 nm to enable a comparison with other studies shown in Figure 3. A plot of AOD at 1020.9 and 1636 nm with AERONET at 1020 and 1640 nm can be found in the Figure B3.

Table B1. Mean values of ln(Vo) from September 14, 19, and 24, 2020 used for deriving AOD.

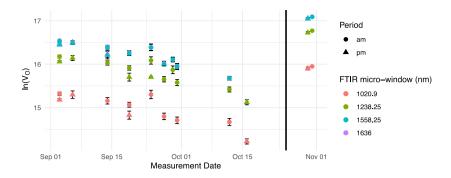| Window	Mean ln(Vo)	sd	n
1020.9	15.17	0.11	3
1238.25	16.01	0.09	3
1558.25	16.34	0.08	3
1636	16.35	0.08	3

615

23

Figure B1. Absolute calibration for Langley exponential analysis of the EM27/SUN solar spectra over time from September to November 2020. Mirrors became significantly dirtier and dustier over the course of the measurement period. The ln(Vo) increased considerably after instrument mirrors were cleaned after the field campaign ended (black line).
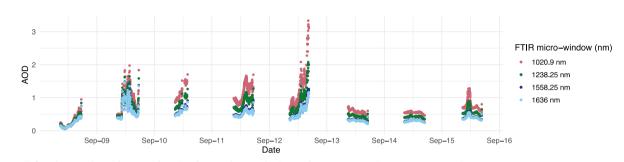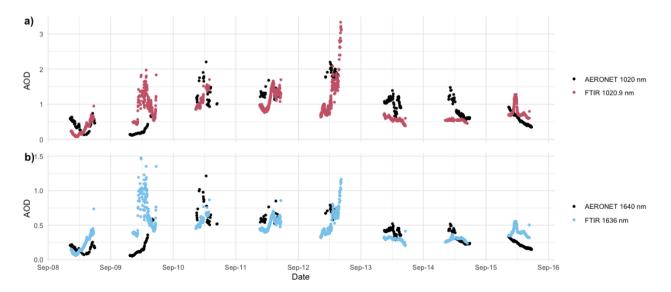
620

Figure B2. Timeseries of AOD for the four micro-windows from September 8 to September 15, 2020.

625 **Figure B3.** Timeseries of AOD from FTIR for the a) 1020.9 (red) and b) 1636 (blue) nm windows and AERONET (black) located in Fresno, CA ~90 km north of measurement site.

24

Appendix C: EM27/SUN Sensitivity

630   The EM27/SUN has different instrument sensitivities defined by the averaging kernels (AK) for each species measured shown below in Figure C1. The difference in sensitivity for the trace gases may introduce a bias in calculated ERs and MCE. Most of the difference is expected to be at the height of the plume where the smoke is concentrated at 4.1 km (~600 hPa). Following the methods of Hedelius et al. (2018), we divide the enhancements of ΔX_{CO2} and ΔX_{CO} by the averaging kernel at that smoke plume height:

635
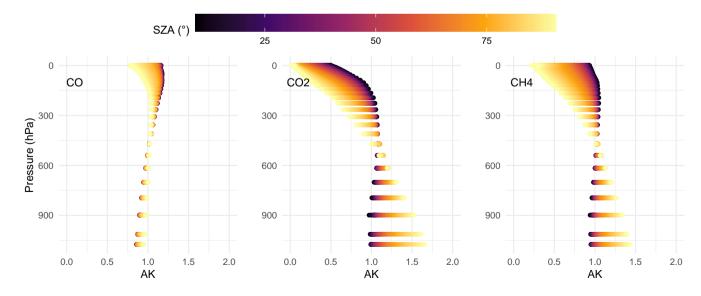
$$MCE_{AK\ corrected}\ (SZA) = \frac{\Delta X_{CO2}\ /\ AK(SZA)_{CO2,600\ hPa}}{\Delta X_{CO2}/AK(SZA)_{CO2,600\ hPa} + \Delta X_{CO}/AK(SZA)_{CO,600\ hPa}} \qquad \text{(Eq. C1)}$$

where $AK_{600\ hPa}$ is the averaging kernel sensitivity for CO or CO_2 as a function of SZA. The mean relative difference of the correction for the Sept. 12 plume event is -1.1%, thus not applying this correction would overestimate the MCE by 1.1%

640   Similarly for the ERs, we correct the enhancements prior to fitting the points with a linear regression for the Sept. 12 plume event:

$$ER_{i,AK\ corrected} = \frac{\Delta X_i/AK(SZA)_{i,600\ hPa}}{\Delta X_{CO2}/AK(SZA)_{CO2,600\ hPa}}. \qquad \text{(Eq. C2)}$$

645   Without applying this correction, E_{CH4} would be underestimated by 9.5% and E_{CO} by 14.2% due to the difference in sensitivity.

Figure C1. Averaging kernel (AK) of EM27/SUN of X_{CO} and X_{CO2} colored by solar zenith angle (SZA).

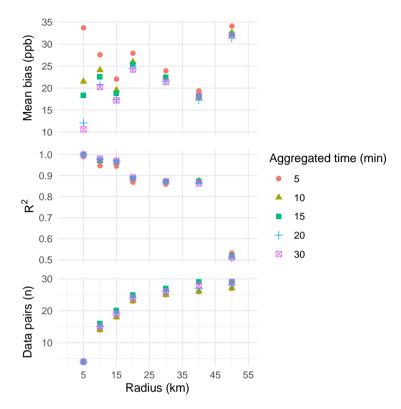**Appendix D: TROPOMI and EM27/SUN Coincident Criteria Sensitivity Analysis**

Figure D1. Results from the sensitivity analysis between the EM27/SUN and TROPOMI with varying radius away from measurement site and varying aggregated times.

655

660

665

Appendix E: Methane from wildfires

Table E1. Emissions of the 20 largest wildfires of 2020 in California. Estimates of CO_2 were obtained from CARB (2020). Emission ratios for Sierra Nevada fires (Creek, Castle, and North Complex) were derived from EF_{CH4} compiled in this study. The rest of the ER_{CH4} are obtained from Xu et al. (2022) that are based on values from Prichard et al. (2020). (Prichard et al., 2020; Xu et al., 2022)

Fire Name	General Vegetation	Wildfire Area Burned (acres)	CO_2 (Tg)	ER_{CH4}	CH4 (Gg)
August Complex	Temperate evergreen	1,032,700	27.7	0.0055 ± 0.0044	55.4 ± 44.3
SCU Complex	Grasslands and savanna	396,399	4.6	0.0043 ± 0.0028	7.2 ± 4.7
Creek	Temperate evergreen	379,882	13.8	0.0084 ± 0.0022	42.2 ± 11
North Complex	Temperate evergreen	318,777	10.9	0.0084 ± 0.0022	33.3 ± 8.7
Hennessey	Shrublands	305,352	3.5	0.0033 ± 0.0021	4.2 ± 2.7
Castle	Temperate evergreen	170,648	6.4	0.0084 ± 0.0022	19.5 ± 5.1
Slater	Temperate evergreen	157,430	6.7	0.0055 ± 0.0044	13.4 ± 10.7
Red Salmon Complex	Temperate evergreen	143,836	4.6	0.0055 ± 0.0044	9.2 ± 7.4
Dolan	Shrublands	124,527	2.1	0.0033 ± 0.0021	2.5 ± 1.6
Bobcat	Shrublands	115,998	2.5	0.0033 ± 0.0021	3.0 ± 1.9
CZU Complex	Temperate evergreen	86,553	5.4	0.0055 ± 0.0044	10.8 ± 8.6
W-5 Cold Springs	Grasslands and savanna	84,817	0.7	0.0043 ± 0.0028	1.1 ± 0.7
Caldwell	Grasslands and savanna	81,224	0.4	0.0043 ± 0.0028	0.6 ± 0.4
Glass	Shrublands	67,484	1.9	0.0033 ± 0.0021	2.3 ± 1.4
Zogg	Shrublands	56,338	0.7	0.0033 ± 0.0021	0.8 ± 0.5
Wallbridge	Shrublands	55,209	4.1	0.0033 ± 0.0021	4.9 ± 3.1
River	Shrublands	50,214	0.9	0.0033 ± 0.0021	1.1 ± 0.7
Loyalton	Grasslands and savanna	46,721	0.7	0.0043 ± 0.0028	1.1 ± 0.7
Dome	Shrublands	44,211	0.1	0.0033 ± 0.0021	0.1 ± 0.1
Apple	Shrublands	33,209	0.8	0.0033 ± 0.0021	1.0 ± 0.6
Total					**213.7 ± 49.8**

References

Adams, C., McLinden, C. A., Shephard, M. W., Dickson, N., Dammers, E., Chen, J., Makar, P., Cady-Pereira, K. E., Tam, N., Kharol, S. K., Lamsal, L. N., and Krotkov, N. A.: Satellite-derived emissions of carbon monoxide, ammonia, and nitrogen dioxide from the 2016 Horse River wildfire in the Fort McMurray area, Atmos. Chem. Phys., 19, 2577–2599, https://doi.org/10.5194/acp-19-2577-2019, 2019.

Aguilera, R., Corringham, T., Gershunov, A., and Benmarhnia, T.: Wildfire smoke impacts respiratory health more than fine particles from other sources: observational evidence from Southern California, Nat Commun, 12, 1493, https://doi.org/10.1038/s41467-021-21708-0, 2021.

Ahangar, F., Cobian-Iñiguez, J., and Cisneros, R.: Combining Regulatory Instruments and Low-Cost Sensors to Quantify the Effects of 2020 California Wildfires on PM2.5 in San Joaquin Valley, Fire, 5, 64, https://doi.org/10.3390/fire5030064, 2022.

Akagi, S. K., Yokelson, R. J., Wiedinmyer, C., Alvarado, M. J., Reid, J. S., Karl, T., Crounse, J. D., and Wennberg, P. O.: Emission factors for open and domestic biomass burning for use in atmospheric models, Atmos. Chem. Phys., 11, 4039–4072, https://doi.org/10.5194/acp-11-4039-2011, 2011.

Alberti, C., Hase, F., Frey, M., Dubravica, D., Blumenstock, T., Dehn, A., Castracane, P., Surawicz, G., Harig, R., Baier, B. C., Bès, C., Bi, J., Boesch, H., Butz, A., Cai, Z., Chen, J., Crowell, S. M., Deutscher, N. M., Ene, D., Franklin, J. E., García, O., Griffith, D., Grouiez, B., Grutter, M., Hamdouni, A., Houweling, S., Humpage, N., Jacobs, N., Jeong, S., Joly, L., Jones, N. B., Jouglet, D., Kivi, R., Kleinschek, R., Lopez, M., Medeiros, D. J., Morino, I., Mostafavipak, N., Müller, A., Ohyama, H., Palmer, P. I., Pathakoti, M., Pollard, D. F., Raffalski, U., Ramonet, M., Ramsay, R., Sha, M. K., Shiomi, K., Simpson, W., Stremme, W., Sun, Y., Tanimoto, H., Té, Y., Tsidu, G. M., Velazco, V. A., Vogel, F., Watanabe, M., Wei, C., Wunch, D., Yamasoe, M., Zhang, L., and Orphal, J.: Improved calibration procedures for the EM27/SUN spectrometers of the COllaborative Carbon Column Observing Network (COCCON), Atmos. Meas. Tech., 15, 2433–2463, https://doi.org/10.5194/amt-15-2433-2022, 2022a.

Alberti, C., Tu, Q., Hase, F., Makarova, M. V., Gribanov, K., Foka, S. C., Zakharov, V., Blumenstock, T., Buchwitz, M., Diekmann, C., Ertl, B., Frey, M. M., Imhasin, H. Kh., Ionov, D. V., Khosrawi, F., Osipov, S. I., Reuter, M., Schneider, M., and Warneke, T.: Investigation of spaceborne trace gas products over St Petersburg and Yekaterinburg, Russia, by using COllaborative Column Carbon Observing Network (COCCON) observations, Atmos. Meas. Tech., 15, 2199–2229, https://doi.org/10.5194/amt-15-2199-2022, 2022b.

Andreae, M. O.: Emission of trace gases and aerosols from biomass burning – an updated assessment, Atmos. Chem. Phys., 19, 8523–8546, https://doi.org/10.5194/acp-19-8523-2019, 2019.

Bader, W., Bovy, B., Conway, S., Strong, K., Smale, D., Turner, A. J., Blumenstock, T., Boone, C., Collaud Coen, M., Coulon, A., Garcia, O., Griffith, D. W. T., Hase, F., Hausmann, P., Jones, N., Krummel, P., Murata, I., Morino, I., Nakajima, H., O'Doherty, S., Paton-Walsh, C., Robinson, J., Sandrin, R., Schneider, M., Servais, C., Sussmann, R., and Mahieu, E.: The recent increase of atmospheric methane from 10 years of ground-based NDACC FTIR observations since 2005, Atmos. Chem. Phys., 17, 2255–2277, https://doi.org/10.5194/acp-17-2255-2017, 2017.

Burling, I. R., Yokelson, R. J., Griffith, D. W. T., Johnson, T. J., Veres, P., Roberts, J. M., Warneke, C., Urbanski, S. P., Reardon, J., Weise, D. R., Hao, W. M., and de Gouw, J.: Laboratory measurements of trace gas emissions from biomass burning of fuel types from the southeastern and southwestern United States, Atmos. Chem. Phys., 10, 11115–11130, https://doi.org/10.5194/acp-10-11115-2010, 2010.

Burling, I. R., Yokelson, R. J., Akagi, S. K., Urbanski, S. P., Wold, C. E., Griffith, D. W. T., Johnson, T. J., Reardon, J., and Weise, D. R.: Airborne and ground-based measurements of the trace gases and particles emitted by prescribed fires in the United States, Atmos. Chem. Phys., 11, 12197–12216, https://doi.org/10.5194/acp-11-12197-2011, 2011.

CARB: California Wildfire Emission Estimates, https://ww2.arb.ca.gov/wildfire-emissions, 2020.

CARB: California Carbon Dioxide Inventory for 2000-2020, https://ww2.arb.ca.gov/sites/default/files/classic/cc/inventory/ghg_inventory_scopingplan_2000-20co2.pdf, 2022a.

CARB: California Methane Inventory for 2000-2020, https://ww2.arb.ca.gov/sites/default/files/classic/cc/inventory/ghg_inventory_scopingplan_2000-20ch4.pdf, 2022b.

Chen, J., Viatte, C., Hedelius, J. K., Jones, T., Franklin, J. E., Parker, H., Gottlieb, E. W., Wennberg, P. O., Dubey, M. K., and Wofsy, S. C.: Differential column measurements using compact solar-tracking spectrometers, Atmos. Chem. Phys., 16, 8479–8498, https://doi.org/10.5194/acp-16-8479-2016, 2016.

Chen, X., Wang, J., Xu, X., Zhou, M., Zhang, H., Castro Garcia, L., Colarco, P. R., Janz, S. J., Yorks, J., McGill, M., Reid, J. S., de Graaf, M., and Kondragunta, S.: First retrieval of absorbing aerosol height over dark target using TROPOMI oxygen B band: Algorithm development and application for surface particulate matter estimates, Remote Sensing of Environment, 265, 112674, https://doi.org/10.1016/j.rse.2021.112674, 2021.

Cho, C., Kim, S.-W., Choi, W., and Kim, M.-H.: Significant light absorption of brown carbon during the 2020 California wildfires, Science of The Total Environment, 813, 152453, https://doi.org/10.1016/j.scitotenv.2021.152453, 2022.

De Mazière, M., Thompson, A. M., Kurylo, M. J., Wild, J. D., Bernhard, G., Blumenstock, T., Braathen, G. O., Hannigan, J. W., Lambert, J.-C., Leblanc, T., McGee, T. J., Nedoluha, G., Petropavlovskikh, I., Seckmeyer, G., Simon, P. C., Steinbrecht, W., and Strahan, S. E.: The Network for the Detection of Atmospheric Composition Change (NDACC): history, status and perspectives, Atmos. Chem. Phys., 18, 4935–4964, https://doi.org/10.5194/acp-18-4935-2018, 2018.

Dietrich, F., Chen, J., Voggenreiter, B., Aigner, P., Nachtigall, N., and Reger, B.: MUCCnet: Munich Urban Carbon Column network, Atmos. Meas. Tech., 14, 1111–1126, https://doi.org/10.5194/amt-14-1111-2021, 2021.

Freeborn, P. H., Jolly, W. M., Cochrane, M. A., and Roberts, G.: Large wildfire driven increases in nighttime fire activity observed across CONUS from 2003–2020, Remote Sensing of Environment, 268, 112777, https://doi.org/10.1016/j.rse.2021.112777, 2022.

Frey, M., Sha, M. K., Hase, F., Kiel, M., Blumenstock, T., Harig, R., Surawicz, G., Deutscher, N. M., Shiomi, K., Franklin, J. E., Bösch, H., Chen, J., Grutter, M., Ohyama, H., Sun, Y., Butz, A., Mengistu Tsidu, G., Ene, D., Wunch, D., Cao, Z., Garcia, O., Ramonet, M., Vogel, F., and Orphal, J.: Building the COllaborative Carbon Column Observing Network (COCCON): long-term stability and ensemble performance of the EM27/SUN Fourier transform spectrometer, Atmos. Meas. Tech., 12, 1513–1530, https://doi.org/10.5194/amt-12-1513-2019, 2019.

Giles, D. M., Sinyuk, A., Sorokin, M. G., Schafer, J. S., Smirnov, A., Slutsker, I., Eck, T. F., Holben, B. N., Lewis, J. R., Campbell, J. R., Welton, E. J., Korkin, S. V., and Lyapustin, A. I.: Advancements in the Aerosol Robotic Network (AERONET) Version 3 database – automated near-real-time quality control algorithm with improved cloud screening for Sun photometer aerosol optical depth (AOD) measurements, Atmos. Meas. Tech., 41, 2019.

Griffin, D., McLinden, C. A., Dammers, E., Adams, C., Stockwell, C., Warneke, C., Bourgeois, I., Peischl, J., Ryerson, T. B., Zarzana, K. J., Rowe, J. P., Volkamer, R., Knote, C., Kille, N., Koenig, T. K., Lee, C. F., Rollins, D., Rickly, P. S., Chen, J., Fehr, L., Bourassa, A., Degenstein, D., Hayden, K., Mihele, C., Wren, S. N., Liggio, J., Akingunola, A., and Makar, P.:

Biomass burning nitrogen dioxide emissions derived from space with TROPOMI: methodology and validation, Gases/Remote Sensing/Validation and Intercomparisons, https://doi.org/10.5194/amt-2021-223, 2021.

785   Gutierrez, A. A., Hantson, S., Langenbrunner, B., Chen, B., Jin, Y., Goulden, M. L., and Randerson, J. T.: Wildfire response to changing daily temperature extremes in California's Sierra Nevada, Sci. Adv., 7, eabe6417, https://doi.org/10.1126/sciadv.abe6417, 2021.

Hase, F., Frey, M., Kiel, M., Blumenstock, T., Harig, R., Keens, A., and Orphal, J.: Addition of a channel for XCO observations to a portable FTIR spectrometer for greenhouse gas measurements, Atmos. Meas. Tech., 9, 2303–2313, 790   https://doi.org/10.5194/amt-9-2303-2016, 2016.

Hedelius, J. K., Viatte, C., Wunch, D., Roehl, C. M., Toon, G. C., Chen, J., Jones, T., Wofsy, S. C., Franklin, J. E., Parker, H., Dubey, M. K., and Wennberg, P. O.: Assessment of errors and biases in retrievals of XCO2, XCH4, XCO, and XN2O from a 0.5 cm−1 resolution solar-viewing spectrometer, Atmos. Meas. Tech., 20, 2016.

Heerah, S., Frausto-Vicencio, I., Jeong, S., Marklein, A. R., Ding, Y., Meyer, A. G., Parker, H. A., Fischer, M. L., Franklin, J. 795   E., Hopkins, F. M., and Dubey, M.: Dairy Methane Emissions in California's San Joaquin Valley Inferred With Ground-Based Remote Sensing Observations in the Summer and Winter, JGR Atmospheres, 126, https://doi.org/10.1029/2021JD034785, 2021.

Herrera, S. A., Diskin, G. S., Harward, C., Sachse, G., De Wekker, S. F. J., Yang, M., Choi, Y., Wisthaler, A., Mallia, D. V., and Pusede, S. E.: Wintertime Nitrous Oxide Emissions in the San Joaquin Valley of California Estimated from Aircraft 800   Observations, Environ. Sci. Technol., 55, 4462–4473, https://doi.org/10.1021/acs.est.0c08418, 2021.

IPCC: Climate Change 2021: The Physical Science Basis. Contribution of Working Group I to the Sixth Assessment Report of the Intergovernmental Panel on Climate Change, edited by: Masson-Delmotte, V., Zhai, P., Pirani, A., Connors, S. L., Pean, C., Berger, S., Caud, N., Chen, Y., Goldfarb, L., Gomis, M. I., Huang, M., Leitzell, K., Lonnoy, E., Matthews, T. K., Waterfield, T., Yelekçi, Ö., Yu, R., and Zhou, B., Cambridge University Press, Cambridge, United Kingdom and New York, 805   NY, USA, 2391 pp., 2021.

Jacobs, N.: Vetting Model and Satellite-Based Estimates of Regional Scale Carbon Exchange at Northern High Latitudes Using Solar-Viewing Infrared Spectroscopy, ProQuest Dissertations Publishing, 2021.

Jain, P., Castellanos-Acuna, D., Coogan, S. C. P., Abatzoglou, J. T., and Flannigan, M. D.: Observed increases in extreme fire weather driven by atmospheric humidity and temperature, Nat. Clim. Chang., 12, 63–70, https://doi.org/10.1038/s41558-021- 810   01224-1, 2022.

Jin, X., Zhu, Q., and Cohen, R.: Direct estimates of biomass burning NO_x emissions and lifetime using daily observations from TROPOMI, Gases/Remote Sensing/Troposphere/Chemistry (chemical composition and reactions), https://doi.org/10.5194/acp-2021-381, 2021.

Kalnay, E., Kanamitsu, M., Kistler, R., Collins, W., Deaven, D., Gandin, L., Iredell, M., Saha, S., White, G., Woollen, J., Zhu, 815   Y., Chelliah, M., Ebisuzaki, W., Higgins, W., Janowiak, J., Mo, K. C., Ropelewski, C., Wang, J., Leetmaa, A., Reynolds, R., Jenne, R., and Joseph, D.: The NCEP/NCAR 40-Year Reanalysis Project, Bulletin of the American Meteorological Society, 77, 437–472, https://doi.org/10.1175/1520-0477(1996)077<0437:TNYRP>2.0.CO;2, 1996.

Kampe, T. U. and Sokolik, I. N.: Remote sensing retrievals of fine mode aerosol optical depth and impacts on its correlation with CO from biomass burning, Geophys. Res. Lett., 34, L12806, https://doi.org/10.1029/2007GL029805, 2007.

Kille, N., Zarzana, K. J., Alvarez, J. R., Lee, C. F., Rowe, J. P., Howard, B., Campos, T., Hills, A., Hornbrook, R. S., Ortega, I., Permar, W., Ku, I. T., Lindaas, J., Pollack, I. B., Sullivan, A. P., Zhou, Y., Fredrickson, C. D., Palm, B. B., Peng, Q., Apel, E. C., Hu, L., Collett, J. L., Fischer, E. V., Flocke, F., Hannigan, J. W., Thornton, J., and Volkamer, R.: The CU Airborne Solar Occultation Flux Instrument: Performance Evaluation during BB-FLUX, ACS Earth and Space Chemistry, 15, 2022.

Lasslop, G., Coppola, A. I., Voulgarakis, A., Yue, C., and Veraverbeke, S.: Influence of Fire on the Carbon Cycle and Climate, Curr Clim Change Rep, 5, 112–123, https://doi.org/10.1007/s40641-019-00128-9, 2019.

Li, M., Karu, E., Brenninkmeijer, C., Fischer, H., Lelieveld, J., and Williams, J.: Tropospheric OH and stratospheric OH and Cl concentrations determined from CH4, CH3Cl, and SF6 measurements, npj Clim Atmos Sci, 1, 1–7, https://doi.org/10.1038/s41612-018-0041-9, 2018.

Lindenmaier, R., Dubey, M. K., Henderson, B. G., Butterfield, Z. T., Herman, J. R., Rahn, T., and Lee, S.-H.: Multiscale observations of CO_2, $^{13}CO_2$, and pollutants at Four Corners for emission verification and attribution, Proc. Natl. Acad. Sci. U.S.A., 111, 8386–8391, https://doi.org/10.1073/pnas.1321883111, 2014.

Liu, X., Huey, L. G., Yokelson, R. J., Selimovic, V., Simpson, I. J., Müller, M., Jimenez, J. L., Campuzano-Jost, P., Beyersdorf, A. J., Blake, D. R., Butterfield, Z., Choi, Y., Crounse, J. D., Day, D. A., Diskin, G. S., Dubey, M. K., Fortner, E., Hanisco, T. F., Hu, W., King, L. E., Kleinman, L., Meinardi, S., Mikoviny, T., Onasch, T. B., Palm, B. B., Peischl, J., Pollack, I. B., Ryerson, T. B., Sachse, G. W., Sedlacek, A. J., Shilling, J. E., Springston, S., St. Clair, J. M., Tanner, D. J., Teng, A. P., Wennberg, P. O., Wisthaler, A., and Wolfe, G. M.: Airborne measurements of western U.S. wildfire emissions: Comparison with prescribed burning and air quality implications, JGR Atmospheres, 122, 6108–6129, https://doi.org/10.1002/2016JD026315, 2017.

Lobert, J. M.: Trace gases and air mass origin at Kaashidhoo, Indian Ocean, J. Geophys. Res., 107, 8013, https://doi.org/10.1029/2001JD000731, 2002.

Lueker, T. J., Keeling, R. F., and Dubey, M. K.: The oxygen to carbon dioxide ratios observed in emissions from a wildfire in northern California, Geophys. Res. Lett., 28, 2413–2416, https://doi.org/10.1029/2000GL011860, 2001.

Lutsch, E., Dammers, E., Conway, S., and Strong, K.: Long-range transport of NH_3, CO, HCN, and C_2H_6 from the 2014 Canadian Wildfires: CANADIAN WILDFIRE EMISSIONS OF NH_3, Geophys. Res. Lett., 43, 8286–8297, https://doi.org/10.1002/2016GL070114, 2016.

Lutsch, E., Strong, K., Jones, D. B. A., Blumenstock, T., Conway, S., Fisher, J. A., Hannigan, J. W., Hase, F., Kasai, Y., Mahieu, E., Makarova, M., Morino, I., Nagahama, T., Notholt, J., Ortega, I., Palm, M., Poberovskii, A. V., Sussmann, R., and Warneke, T.: Detection and attribution of wildfire pollution in the Arctic and northern midlatitudes using a network of Fourier-transform infrared spectrometers and GEOS-Chem, Atmos. Chem. Phys., 20, 12813–12851, https://doi.org/10.5194/acp-20-12813-2020, 2020.

Makarova, M. V., Alberti, C., Ionov, D. V., Hase, F., Foka, S. C., Blumenstock, T., Warneke, T., Virolainen, Y. A., Kostsov, V. S., Frey, M., Poberovskii, A. V., Timofeyev, Y. M., Paramonova, N. N., Volkova, K. A., Zaitsev, N. A., Biryukov, E. Y., Osipov, S. I., Makarov, B. K., Polyakov, A. V., Ivakhov, V. M., Imhasin, H. Kh., and Mikhailov, E. F.: Emission Monitoring Mobile Experiment (EMME): an overview and first results of the St. Petersburg megacity campaign 2019, Atmos. Meas. Tech., 14, 1047–1073, https://doi.org/10.5194/amt-14-1047-2021, 2021.

Marklein, A. R., Meyer, D., Fischer, M. L., Jeong, S., Rafiq, T., Carr, M., and Hopkins, F. M.: Facility-scale inventory of dairy methane emissions in California: implications for mitigation, Earth Syst. Sci. Data, 13, 1151–1166, https://doi.org/10.5194/essd-13-1151-2021, 2021.

McKain, K., Down, A., Raciti, S. M., Budney, J., Hutyra, L. R., Floerchinger, C., Herndon, S. C., Nehrkorn, T., Zahniser, M. S., Jackson, R. B., Phillips, N., and Wofsy, S. C.: Methane emissions from natural gas infrastructure and use in the urban region of Boston, Massachusetts, Proc. Natl. Acad. Sci. U.S.A., 112, 1941–1946, https://doi.org/10.1073/pnas.1416261112, 2015.

McMillan, W. W., Warner, J. X., Comer, M. M., Maddy, E., Chu, A., Sparling, L., Eloranta, E., Hoff, R., Sachse, G., Barnet, C., Razenkov, I., and Wolf, W.: AIRS views transport from 12 to 22 July 2004 Alaskan/Canadian fires: Correlation of AIRS CO and MODIS AOD with forward trajectories and comparison of AIRS CO retrievals with DC-8 in situ measurements during INTEX-A/ICARTT, J. Geophys. Res., 113, D20301, https://doi.org/10.1029/2007JD009711, 2008.

Moody, T. J., Fites-Kaufman, J., and Stephens, S. L.: Fire history and climate influences from forests in the Northern Sierra Nevada, USA, fire ecol, 2, 115–141, https://doi.org/10.4996/fireecology.0201115, 2006.

Morris III, G. and Dennis, C.: 2020 Fire Siege, CALFIRE, 2020.

Navarro, K. M., Cisneros, R., and Balmes, J. R.: Air-Quality Impacts and Intake Fraction of PM2.5 during the 2013 Rim Megafire, Environ. Sci. Technol., 9, 2016.

Paton-Walsh, C., Jones, N. B., Wilson, S. R., Haverd, V., Meier, A., Griffith, D. W. T., and Rinsland, C. P.: Measurements of trace gas emissions from Australian forest fires and correlations with coincident measurements of aerosol optical depth, J. Geophys. Res., 110, D24305, https://doi.org/10.1029/2005JD006202, 2005.

Prichard, S. J., O'Neill, S. M., Eagle, P., Andreu, A. G., Drye, B., Dubowy, J., Urbanski, S., and Strand, T. M.: Wildland fire emission factors in North America: synthesis of existing data, measurement needs and management applications, Int. J. Wildland Fire, 29, 132, https://doi.org/10.1071/WF19066, 2020.

Reinhardt, E. D. and Dickinson, M. B.: First-Order Fire Effects Models for Land Management: Overview and Issues, fire ecol, 6, 131–142, https://doi.org/10.4996/fireecology.0601131, 2010.

Sagar, V. K., Pathakoti, M., D.V., M., K.S., R., M.V.R., S. S., Hase, F., Dubravica, D., and Sha, M. K.: Ground-Based Remote Sensing of Total Columnar CO_2, CH_4, and CO Using EM27/SUN FTIR Spectrometer at a Suburban Location (Shadnagar) in India and Validation of Sentinel-5P/TROPOMI, IEEE Geosci. Remote Sensing Lett., 19, 1–5, https://doi.org/10.1109/LGRS.2022.3171216, 2022.

Saunois, M., Stavert, A. R., Poulter, B., Bousquet, P., Canadell, J. G., Jackson, R. B., Raymond, P. A., Dlugokencky, E. J., Houweling, S., Patra, P. K., Ciais, P., Arora, V. K., Bastviken, D., Bergamaschi, P., Blake, D. R., Brailsford, G., Bruhwiler, L., Carlson, K. M., Carrol, M., Castaldi, S., Chandra, N., Crevoisier, C., Crill, P. M., Covey, K., Curry, C. L., Etiope, G., Frankenberg, C., Gedney, N., Hegglin, M. I., Höglund-Isaksson, L., Hugelius, G., Ishizawa, M., Ito, A., Janssens-Maenhout, G., Jensen, K. M., Joos, F., Kleinen, T., Krummel, P. B., Langenfelds, R. L., Laruelle, G. G., Liu, L., Machida, T., Maksyutov, S., McDonald, K. C., McNorton, J., Miller, P. A., Melton, J. R., Morino, I., Müller, J., Murguia-Flores, F., Naik, V., Niwa, Y., Noce, S., O'Doherty, S., Parker, R. J., Peng, C., Peng, S., Peters, G. P., Prigent, C., Prinn, R., Ramonet, M., Regnier, P., Riley, W. J., Rosentreter, J. A., Segers, A., Simpson, I. J., Shi, H., Smith, S. J., Steele, L. P., Thornton, B. F., Tian, H., Tohjima, Y., Tubiello, F. N., Tsuruta, A., Viovy, N., Voulgarakis, A., Weber, T. S., van Weele, M., van der Werf, G. R., Weiss, R. F., Worthy, D., Wunch, D., Yin, Y., Yoshida, Y., Zhang, W., Zhang, Z., Zhao, Y., Zheng, B., Zhu, Q., Zhu, Q., and Zhuang, Q.: The Global Methane Budget 2000–2017, Earth Syst. Sci. Data, 12, 1561–1623, https://doi.org/10.5194/essd-12-1561-2020, 2020.

Schneising, O., Buchwitz, M., Reuter, M., Bovensmann, H., and Burrows, J. P.: Severe Californian wildfires in November 2018 observed from space: the carbon monoxide perspective, Atmos. Chem. Phys., 20, 3317–3332, https://doi.org/10.5194/acp-20-3317-2020, 2020.

Scholl, A. E. and Taylor, A. H.: Fire regimes, forest change, and self-organization in an old-growth mixed-conifer forest, Yosemite National Park, USA, Ecological Applications, 20, 362–380, https://doi.org/10.1890/08-2324.1, 2010.

Sha, M. K., Langerock, B., Blavier, J.-F. L., Blumenstock, T., Borsdorff, T., Buschmann, M., Dehn, A., De Mazière, M., Deutscher, N. M., Feist, D. G., García, O. E., Griffith, D. W. T., Grutter, M., Hannigan, J. W., Hase, F., Heikkinen, P., Hermans, C., Iraci, L. T., Jeseck, P., Jones, N., Kivi, R., Kumps, N., Landgraf, J., Lorente, A., Mahieu, E., Makarova, M. V., Mellqvist, J., Metzger, J.-M., Morino, I., Nagahama, T., Notholt, J., Ohyama, H., Ortega, I., Palm, M., Petri, C., Pollard, D. F., Rettinger, M., Robinson, J., Roche, S., Roehl, C. M., Röhling, A. N., Rousogenous, C., Schneider, M., Shiomi, K., Smale, D., Stremme, W., Strong, K., Sussmann, R., Té, Y., Uchino, O., Velazco, V. A., Vigouroux, C., Vrekoussis, M., Wang, P., Warneke, T., Wizenberg, T., Wunch, D., Yamanouchi, S., Yang, Y., and Zhou, M.: Validation of methane and carbon monoxide from Sentinel-5 Precursor using TCCON and NDACC-IRWG stations, Atmos. Meas. Tech., 14, 6249–6304, https://doi.org/10.5194/amt-14-6249-2021, 2021.

Stephensen, N. and Brigham, C.: Preliminary Estimates of Sequoia Mortality in the 2020 Castle Fire (U.S. National Park Service), https://www.nps.gov/articles/000/preliminary-estimates-of-sequoia-mortality-in-the-2020-castle-fire.htm, 2021.

Toon, G., Blavier, J.-F., Washenfelder, R., Wunch, D., Keppel-Aleks, G., Wennberg, P., Connor, B., Sherlock, V., Griffith, D., Deutscher, N., and Notholt, J.: Total Column Carbon Observing Network (TCCON), in: Advances in Imaging, Fourier Transform Spectroscopy, Vancouver, JMA3, https://doi.org/10.1364/FTS.2009.JMA3, 2009.

UNEP: Spreading like Wildfire – The Rising Threat of Extraordinary Landscape Fires, United Nations Environment Programme, Nairobi, 2022.

Urbanski, S.: Wildland fire emissions, carbon, and climate: Emission factors, Forest Ecology and Management, 317, 51–60, https://doi.org/10.1016/j.foreco.2013.05.045, 2014.

Urbanski, S. P.: Combustion efficiency and emission factors for wildfire-season fires in mixed conifer forests of the northern Rocky Mountains, US, Atmos. Chem. Phys., 13, 7241–7262, https://doi.org/10.5194/acp-13-7241-2013, 2013.

Veefkind, J. P., Aben, I., McMullan, K., Förster, H., de Vries, J., Otter, G., Claas, J., Eskes, H. J., de Haan, J. F., Kleipool, Q., van Weele, M., Hasekamp, O., Hoogeveen, R., Landgraf, J., Snel, R., Tol, P., Ingmann, P., Voors, R., Kruizinga, B., Vink, R., Visser, H., and Levelt, P. F.: TROPOMI on the ESA Sentinel-5 Precursor: A GMES mission for global observations of the atmospheric composition for climate, air quality and ozone layer applications, Remote Sensing of Environment, 120, 70–83, https://doi.org/10.1016/j.rse.2011.09.027, 2012.

Viatte, C., Strong, K., Walker, K. A., and Drummond, J. R.: Five years of CO, HCN, C_2H_6, C_2H_2, CH_3OH, HCOOH and H_2CO total columns measured in the Canadian high Arctic, Atmos. Meas. Tech., 7, 1547–1570, https://doi.org/10.5194/amt-7-1547-2014, 2014.

Viatte, C., Strong, K., Hannigan, J., Nussbaumer, E., Emmons, L. K., Conway, S., Paton-Walsh, C., Hartley, J., Benmergui, J., and Lin, J.: Identifying fire plumes in the Arctic with tropospheric FTIR measurements and transport models, Atmos. Chem. Phys., 15, 2227–2246, https://doi.org/10.5194/acp-15-2227-2015, 2015.

Viatte, C., Lauvaux, T., Hedelius, J. K., Parker, H., Chen, J., Jones, T., Franklin, J. E., Deng, A. J., Gaudet, B., Verhulst, K., Duren, R., Wunch, D., Roehl, C., Dubey, M. K., Wofsy, S., and Wennberg, P. O.: Methane emissions from dairies in the Los Angeles Basin, Atmos. Chem. Phys., 17, 7509–7528, https://doi.org/10.5194/acp-17-7509-2017, 2017.

Vogel, F. R., Frey, M., Staufer, J., Hase, F., Broquet, G., Xueref-Remy, I., Chevallier, F., Ciais, P., Sha, M. K., Chelin, P., Jeseck, P., Janssen, C., Té, Y., Groß, J., Blumenstock, T., Tu, Q., and Orphal, J.: XCO2 in an emission hot-spot region: the COCCON Paris campaign 2015, Atmos. Chem. Phys., 19, 3271–3285, https://doi.org/10.5194/acp-19-3271-2019, 2019.

940 van der Werf, G. R., Randerson, J. T., Giglio, L., van Leeuwen, T. T., Chen, Y., Rogers, B. M., Mu, M., van Marle, M. J. E., Morton, D. C., Collatz, G. J., Yokelson, R. J., and Kasibhatla, P. S.: Global fire emissions estimates during 1997–2016, Earth Syst. Sci. Data, 9, 697–720, https://doi.org/10.5194/essd-9-697-2017, 2017.

Whitburn, S., Van Damme, M., Kaiser, J. W., van der Werf, G. R., Turquety, S., Hurtmans, D., Clarisse, L., Clerbaux, C., and Coheur, P.-F.: Ammonia emissions in tropical biomass burning regions: Comparison between satellite-derived emissions and bottom-up fire inventories, Atmospheric Environment, 121, 42–54, https://doi.org/10.1016/j.atmosenv.2015.03.015, 2015.

945 Wiedinmyer, C., Akagi, S. K., Yokelson, R. J., Emmons, L. K., Al-Saadi, J. A., Orlando, J. J., and Soja, A. J.: The Fire INventory from NCAR (FINN): a high resolution global model to estimate the emissions from open burning, Geoscientific Model Development, 4, 625–641, https://doi.org/10.5194/gmd-4-625-2011, 2011.

Wilmot, T. Y., Mallia, D. V., Hallar, A. G., and Lin, J. C.: Wildfire plumes in the Western US are reaching greater heights and injecting more aerosols aloft as wildfire activity intensifies, Sci Rep, 12, 12400, https://doi.org/10.1038/s41598-022-16607-3, 950 2022.

Wunch, D., Wennberg, P. O., Toon, G. C., Keppel-Aleks, G., and Yavin, Y. G.: Emissions of greenhouse gases from a North American megacity: GREENHOUSE GAS EMISSIONS IN LA, Geophys. Res. Lett., 36, n/a-n/a, https://doi.org/10.1029/2009GL039825, 2009.

Wunch, D., Toon, G. C., Blavier, J.-F. L., Washenfelder, R. A., Notholt, J., Connor, B. J., Griffith, D. W. T., Sherlock, V., and 955 Wennberg, P. O.: The Total Carbon Column Observing Network, Phil. Trans. R. Soc. A., 369, 2087–2112, https://doi.org/10.1098/rsta.2010.0240, 2011.

Xu, Q., Westerling, A. L., Notohamiprodjo, A., Wiedinmyer, C., Picotte, J. J., Parks, S. A., Hurteau, M. D., Marlier, M. E., Kolden, C. A., Sam, J. A., Baldwin, W. J., and Ade, C.: Wildfire burn severity and emissions inventory: an example implementation over California, Environ. Res. Lett., 17, 085008, https://doi.org/10.1088/1748-9326/ac80d0, 2022.

960 Yates, E. L., Iraci, L. T., Singh, H. B., Tanaka, T., Roby, M. C., Hamill, P., Clements, C. B., Lareau, N., Contezac, J., Blake, D. R., Simpson, I. J., Wisthaler, A., Mikoviny, T., Diskin, G. S., Beyersdorf, A. J., Choi, Y., Ryerson, T. B., Jimenez, J. L., Campuzano-Jost, P., Loewenstein, M., and Gore, W.: Airborne measurements and emission estimates of greenhouse gases and other trace constituents from the 2013 California Yosemite Rim wildfire, Atmospheric Environment, 127, 293–302, https://doi.org/10.1016/j.atmosenv.2015.12.038, 2016.

965 Yokelson, R. J., Goode, J. G., Ward, D. E., Susott, R. A., Babbitt, R. E., Wade, D. D., Bertschi, I., Griffith, D. W. T., and Hao, W. M.: Emissions of formaldehyde, acetic acid, methanol, and other trace gases from biomass fires in North Carolina measured by airborne Fourier transform infrared spectroscopy, J. Geophys. Res., 104, 30109–30125, https://doi.org/10.1029/1999JD900817, 1999.

Yokelson, R. J., Andreae, M. O., and Akagi, S. K.: Pitfalls with the use of enhancement ratios or normalized excess mixing 970 ratios measured in plumes to characterize pollution sources and aging, Atmos. Meas. Tech., 6, 2155–2158, https://doi.org/10.5194/amt-6-2155-2013, 2013.

Zhuang, Y., Fu, R., Santer, B. D., Dickinson, R. E., and Hall, A.: Quantifying contributions of natural variability and anthropogenic forcings on increased fire weather risk over the western United States, 9, 2021.

Zoogman, P., Liu, X., Suleiman, R. M., Pennington, W. F., Flittner, D. E., Al-Saadi, J. A., Hilton, B. B., Nicks, D. K.,
975   Newchurch, M. J., Carr, J. L., Janz, S. J., Andraschko, M. R., Arola, A., Baker, B. D., Canova, B. P., Chan Miller, C., Cohen, R. C., Davis, J. E., Dussault, M. E., Edwards, D. P., Fishman, J., Ghulam, A., González Abad, G., Grutter, M., Herman, J. R., Houck, J., Jacob, D. J., Joiner, J., Kerridge, B. J., Kim, J., Krotkov, N. A., Lamsal, L., Li, C., Lindfors, A., Martin, R. V., McElroy, C. T., McLinden, C., Natraj, V., Neil, D. O., Nowlan, C. R., O'Sullivan, E. J., Palmer, P. I., Pierce, R. B., Pippin, M. R., Saiz-Lopez, A., Spurr, R. J. D., Szykman, J. J., Torres, O., Veefkind, J. P., Veihelmann, B., Wang, H., Wang, J., and
980   Chance, K.: Tropospheric emissions: Monitoring of pollution (TEMPO), Journal of Quantitative Spectroscopy and Radiative Transfer, 186, 17–39, https://doi.org/10.1016/j.jqsrt.2016.05.008, 2017.

36